Evolution of the *UV* LF from $z \sim 15$ to $z \sim 8$ using new *JWST* NIRCam medium-band observations over the HUDF/XDF

Rychard J. Bouwens,[1][⋆] Mauro Stefanon,[2,3] Gabriel Brammer,[4] Pascal A. Oesch [4,5]
Thomas Herard-Demanche,[1] Garth D. Illingworth,[6] Jorryt Matthee [7] Rohan P. Naidu [8,9]
Pieter G. van Dokkum[10] and Ivana F. van Leeuwen[1]

[1]*Leiden Observatory, Leiden University, NL-2300 RA Leiden, Netherlands*
[2]*Departament d'Astronomia i Astrofísica, Universitat de València, C. Dr Moliner 50, E-46100 Burjassot, València, Spain*
[3]*Unidad Asociada CSIC 'Grupo de Astrofísica Extragaláctica y Cosmología' (Instituto de F ísica de Cantabria – Universitat de València), Parque Científico,
C/ Catedràtic José Beltrán, 2, 46980 Paterna (València), Spain*
[4]*Cosmic Dawn Center (DAWN), Niels Bohr Institute, University of Copenhagen, Jagtvej 128, København N, DK-2200, Denmark*
[5]*Department of Astronomy, University of Geneva, Chemin Pegasi 51, 1290 Versoix, Switzerland*
[6]*UCO/Lick Observatory, University of California, Santa Cruz, CA 95064, USA*
[7]*Department of Physics, ETH Züurich, Wolfgang-Pauli-Strasse 27, 8093 Züurich, Switzerland*
[8]*Center for Astrophysics, Harvard & Smithsonian, 60 Garden Street, Cambridge, MA 02138, USA*
[9]*MIT Kavli Institute for Astrophysics and Space Research, 77 Massachusetts Ave., Cambridge, MA 02139, USA*
[10]*Astronomy Department, Yale University, 52 Hillhouse Ave, New Haven, CT 06511, USA*

ABSTRACT

We present the first constraints on the prevalence of $z > 10$ galaxies in the *Hubble* Ultra Deep Field (HUDF) leveraging new NIRCam observations from JEMS (*JWST* Extragalactic Medium-band Survey). These NIRCam observations probe redward of 1.6 μm, beyond the wavelength limit of *HST*, allowing us to search for galaxies to $z > 10$. These observations indicate that the highest redshift candidate identified in the HUDF09 data with *HST*, UDFj-39546284, has a redshift of $z > 11.5$, as had been suggested in analyses of the HUDF12/XDF data. This has now been confirmed with *JWST* NIRSpec. This source is thus the most distant galaxy discovered by *HST* in its >30 yr of operation. Additionally, we identify nine other $z \sim 8$–13 candidate galaxies over the HUDF, two of which are new discoveries that appear to lie at $z \sim 11$–12. We use these results to characterize the evolution of the *UV* luminosity function (LF) from $z \sim 15$ to $z \sim 8.7$. While our LF results at $z \sim 8.7$ and $z \sim 10.5$ are consistent with previous findings over the HUDF, our new LF estimates at $z \sim 12.6$ are higher than other results in the literature, potentially pointing to a milder evolution in the *UV* luminosity density from $z \sim 12.6$. We emphasize that our LF results are uncertain given the small number of $z \sim 12.6$ sources and limited volume probed. The new NIRCam data also indicate that the faint $z \sim 8$–13 galaxies in the HUDF/XDF show blue *UV*-continuum slopes $\beta \sim -2.7$, high specific star formation rates ~ 24.5 Gyr^{-1}, and high EW (~ 1300 Å) [O III] + H β emission, with two $z \sim 8.5$ sources showing [O III] + H β EWs of ~ 2300 Å.

Key words: galaxies: evolution – galaxies: high-redshift – Cosmology: dark ages, reionization, first stars.

1 INTRODUCTION

One of the most interesting frontiers in extragalactic astronomy concerns the formation and growth of galaxies in the early universe. Significant open questions exist regarding the efficiency of star formation in the early universe (e.g. Behroozi, Wechsler & Conroy 2013; Stefanon et al. 2017), when cosmic reionization began in earnest (e.g. Bouwens et al. 2015b; Robertson et al. 2015; Robertson 2022), and the overall timeline of stellar assembly (e.g. Madau & Dickinson 2014). Leveraging the capabilities of the *Hubble Space Telescope (HST)* and *Spitzer*, significant progress was made in identifying galaxies to $z \sim 11$ (Coe et al. 2013; Oesch et al. 2016; Jiang et al. 2021) and probing the build-up of stellar mass from z

~ 10 (e.g. Stark et al. 2009; González et al. 2011; Duncan et al. 2014; Grazian et al. 2015; Song et al. 2016; Bhatawdekar et al. 2019; Kikuchihara et al. 2020; Furtak et al. 2021; Stefanon et al. 2021, 2023). Now, with the initial studies with the *JWST*, large numbers of galaxies have been identified with redshifts in excess of $z \sim 10$ (e.g. Adams et al. 2023; Atek et al. 2023; Bradley et al. 2022; Castellano et al. 2022; Finkelstein et al. 2022a; Labbe et al. 2023; Naidu et al. 2023; Rodighiero et al. 2023; Yu-Yang Hsiao et al. 2022) with plausible redshifts as high as $z \sim 17$ (e.g. Atek et al. 2023; Donnan et al. 2023; Harikane et al. 2023; Naidu et al. 2022; Yan et al. 2023; Zavala et al. 2023).

In the midst of all the excitement surrounding the discovery of many plausible $z \geq 10$ galaxies, significant questions have persisted regarding how robust various high redshift candidates from *JWST* are. Of concern has been the limited depth of the imaging data just blueward of various putative Lyman breaks, the only modest overlap

⋆ E-mail: bouwens@strw.leidenuniv.nl

between the specific sources that make up various $z \geq 8$ selections,[1] and uncertainties in the calibration of the NIRCam zeropoints (e.g. Adams et al. 2023).

One way to substantially improve the robustness of current $z \geq 8$ selections is to perform these selections over those extragalactic fields with some of the deepest available imaging observations with *HST*, and there is clearly no field with deeper archival observations than the *Hubble* Ultra Deep Field (HUDF). The HUDF has been the target of more than 1000 h of observations with *HST* (Thompson et al. 2005; Beckwith et al. 2006; Bouwens et al. 2011b; Ellis et al. 2013; Illingworth et al. 2013; Koekemoer et al. 2013; Teplitz et al. 2013), probing to 5σ limiting magnitudes ≥ 30 mag in the bluest three optical bands, to ∼30 mag in the F105W band, and to ∼29.5 mag otherwise (F850LP, F125W, F140W, and F160W). This is approximately 2 mag deeper at optical wavelengths than has been available over other fields with early *JWST* observations, e.g. the Cosmic Evolution Early Release Science (CEERS) program (Finkelstein et al. 2017), SMACS0723 (Pontoppidan et al. 2022), or the GLASS parallel field (Treu et al. 2022).

Here we take advantage of sensitive NIRCam imaging data which have just been obtained over the *Hubble* Ultra Deep Field, as part of the sensitive JEMS (*JWST* Extragalactic Medium-band Survey) program (Williams et al. 2023). Imaging observations from the program were obtained just redward of the sensitive Wide Field Camera 3 (WFC3)/IR observations from the HUDF09 and HUDF12 programs (Bouwens et al. 2011b; Ellis et al. 2013) and enable searches for star-forming galaxies over the *Hubble* Ultra Deep Field to even higher redshift than can be readily probed with the WFC3/IR data sets, i.e. to $z > 10$ and out to $z \sim 15$. The observations also allow for a reevaluation of various candidate $z \geq 10$ galaxies that have already been reported over that field and a rederivation of *UV* LF results at $z \geq 8$. Thanks to the depth of the available supporting observations over the *Hubble* Ultra Deep Field (being up to ∼2 mag deeper than available over other fields), we would expect these new *UV* LF results to be more reliable than most earlier determinations with *JWST*.

In Section 2, we describe the combined *JWST* NIRCam plus *HST* imaging data sets available to search for star-forming galaxies over the *Hubble* Ultra Deep Field as well as our procedures for constructing source catalogs and performing photometry. In Section 3, we describe our procedures for identifying star-forming galaxies over the *Hubble* Ultra Deep Field, and then present the samples of sources we derive and compare it to earlier selections. In Section 4, we use our new samples of $z \sim 8–13$ galaxies to quantify the *UV* LF at $z \geq 8$, characterize the evolution with cosmic time, and analyze the stellar populations and line emission from fainter star-forming galaxies at $z \geq 8$. We refer to the *HST* F435W, F606W, F775W, F814W, F850LP, F105W, F125W, F140W, and F160W bands as B_{435}, V_{606}, i_{775}, I_{814}, z_{850}, Y_{105}, J_{125}, JH_{140}, and H_{160}, respectively, for simplicity, and to the *JWST* F182M and F210M bands as HK_{182} and K_{210}, respectively. For convenience, we quote results in terms of the approximate characteristic luminosity $L^*_{z=3}$ derived at $z \sim 3$ by Steidel et al. (1999), Reddy & Steidel (2009), and many other studies. For ease of comparison to other recent extragalactic work, we assume a concordance cosmology with $\Omega_m = 0.3$, $\Omega_\Lambda = 0.7$, and $H_0 = 70$ km s^{-1} Mpc^{-1} throughout. All star formation rate (SFR) and stellar mass results are quoted assuming a Chabrier (2003) initial mass function (IMF). All magnitude measurements are given using

the AB magnitude system (Oke & Gunn 1983) unless otherwise specified.

2 DATA SETS AND PHOTOMETRY

2.1 Data set

Here we make use of the new *JWST* NIRCam observations taken over the *Hubble* Ultra Deep Field as part of the JEMS (*JWST* Extragalactic Medium-band Survey) medium-band program (Williams et al. 2023). Obtained as part of the program were observations in F182M and F210M short wavelength NIRCam channel and F430M, F460M, and F480M observations taken with the longer wavelength NIRCam channel. The F182M, F210M, and F480M observations had total integration times of 7.8 h each, while the total integration times for the F430M and F460M observations were 3.9 h each in duration. The observations were reduced using GRIZLI reduction pipeline adapted to handle *JWST* NIRCam data (Brammer et al. 2023). GRIZLI includes procedures for masking the 'snowball' artefacts and minimizing the impact of 1/*f* noise. Image combination is treated using ASTRODRIZZLE after converting the WCS information in the image headers to use SIP format.

The WFC3/IR and Advanced Camera for Surveys (ACS) images used for our analysis are the XDF images that were generated in 2013 based on all the overlapping *HST* optical and near-IR images that were available at that time and include ∼1000 orbits of data (Illingworth et al. 2013). These images include deep observations in the F435W, F606W, F775W, F814W, and F850LP bands with ACS and F105W, F125W, F140W, and F160W bands with WFC3/IR.

Fig. 1 and Table 1 summarize the 5σ depth of the imaging data sets we utilize for our analysis, and what is striking is how similar the depths of the available near-IR data sets with *HST* are to the depths of the imaging data sets available with *JWST* in the short wavelength channel, both reaching to ∼29.5 mag at 5σ while the depth of the medium-band observations in the longer wavelength channel is 28.2–28.5, sensitive enough to look for prominent line emission from Hα and [O III] + Hβ in galaxies at $z \sim 5.4–6.6$ and $z \sim 7.6–9.3$, respectively (Williams et al. 2023).

We restrict our search to the ∼4.6 arcmin^2 region on the sky that contains both the deepest WFC3/IR observations from the HUDF09 + HUDF12 programs and *JWST*/NIRCam medium-band observations from the JEMS program (Williams et al. 2023). The footprint of our 4.6 arcmin^2 search field relative to HUDF09 + HUDF12 data set, JEMS field, and JADES NIRCam footprint in the GOODS South is shown in Fig. 2. Also indicated are four spectroscopically-confirmed sources from Curtis-Lake et al. (2022) and Robertson et al. (2022).

2.2 Source detection and photometry

For source detection and photometry over the HUDF, we make use of the SEXTRACTOR code (Bertin & Arnouts 1996). Source detection is performed leveraging a square root of χ^2 image (Szalay, Connolly & Szokoly 1999), constructed from the observations in the F140W, F160W, F182W, and F210M bands for our $z \sim 8–9$ and $z \sim 10–11$ selections, observations in the F182W and F210M bands for our $z \sim 12–13$ selection, and F210M band for our $z \sim 14–15$ selection. The various images contributing to the detection image are first PSF-matched to the lowest resolution bandpass F160W prior to coaddition. Colour measurements are made inside small scalable Kron (1980) apertures, using a Kron factor of 1.2. Flux measurements made in the small scalable apertures are corrected
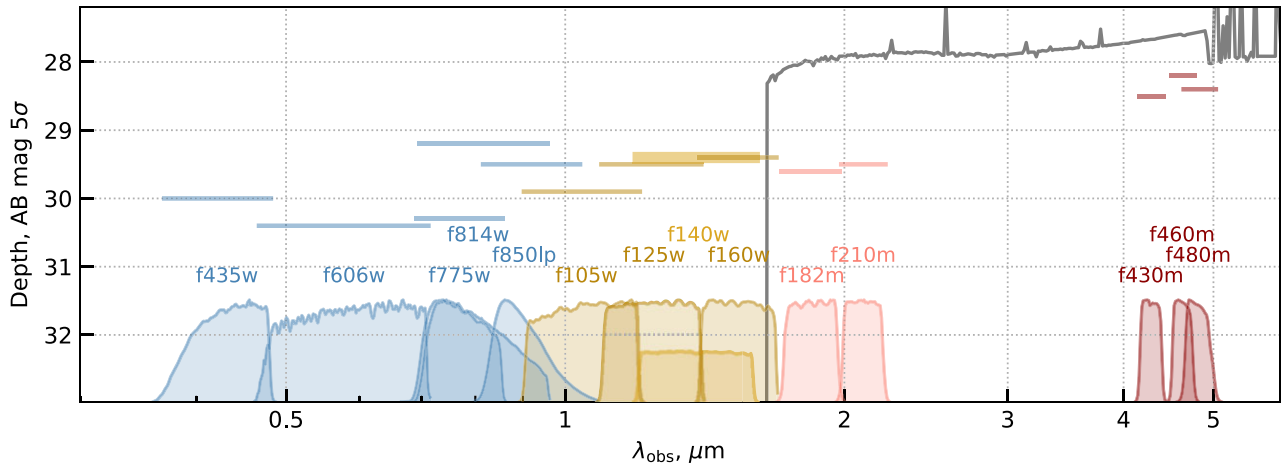

Figure 1. Sensitivity (5σ, AB mag) of the new *JWST* medium band observations in F182M, F210M, F430M, F460M, and F480M (*red horizontal lines*) over the HUDF from the JEMS program (Williams et al. 2023) relative to that available in various filters from the HUDF/XDF optical (*blue lines*) and near-IR (*light brown lines*) observations. Also shown are the wavelength sensitivity curves for the *JWST* medium bands as well as the archival HST observations. For context, a spectral energy distribution (SED) of the $z = 8.5$ galaxy over SMACS0723, as fit with BAGPIPES (Carnall et al. 2018, 2023) and shifted to $z = 12$, is also shown (*grey lines*). Not only are the new *JWST* medium band data well matched to the depth of the archival *HST* HUDF/XDF observations (Illingworth et al. 2013), but they extend the coverage to redder wavelengths, facilitating both an identification of star-forming galaxies over the HUDF to higher redshifts, i.e. $z > 10$, and a characterization of the stellar population and emission line properties of very high-redshift galaxies in the same field.

Table 1. Estimated 5σ depth [in mag] of the *JWST* + *HST* data set we utilize over the HUDF/XDF in 0.35 arcsec diameter apertures.

Band	5σ depth (mag)
HST/F435W	30.0
HST/F606W	30.4
HST/F775W	30.3
HST/F814W	29.2
HST/F850LP	29.5
HST/F105W	29.9
HST/F125W	29.5
HST/F140W	29.4
HST/F160W	29.4
JWST/F182M	29.6
JWST/F210M	29.5
JWST/F430M	28.5
JWST/F460M	28.2
JWST/F480M	28.4
Area [arcmin^2]	4.6

to total by accounting for the additional flux in the square root of χ^2 in larger scalable Kron apertures (Kron factor 2.5) relative to the smaller scalable apertures. An additional correction is made to account for the additional flux at even larger radii than the larger scalable aperture based on the encircled energy in the F210M PSF (typically a ~0.15 mag correction).

3 SOURCE SELECTIONS

3.1 Lyman break selections

As in our previous searches for distant galaxies, we base our selection on the use of two-colour Lyman-break-like criteria. The first colour in a Lyman-break selection ensures that candidate Lyman breaks in sources exceed some minimum amplitude (typically at least 1 mag) while the second colour ensures the intrinsic colours of selected sources are blue. Spectroscopic follow-up of sources identified with
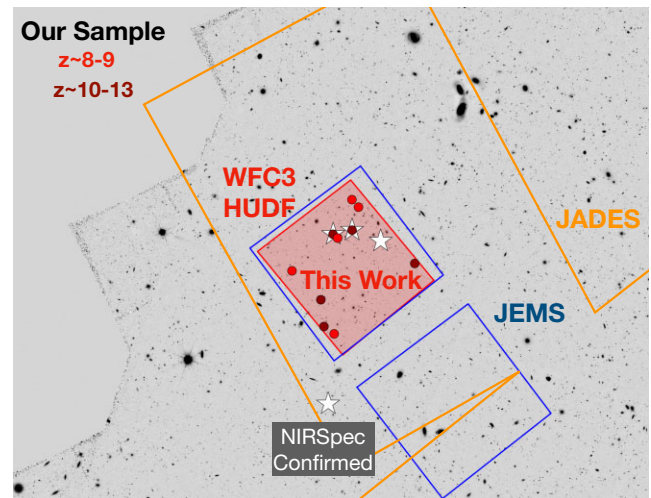

Figure 2. Illustration of our search field (*red shaded region*) for $z \sim 8$–15 galaxies leveraging the deep JEMS medium-band data (*blue rectangles*) and sensitive WFC3/IR data over the HUDF/XDF from HUDF09 + HUDF12 programs (*red rectangle*). The background image shown in greyscale corresponds to the GOODS South *HST* ACS F606W observations (Giavalisco et al. 2004). Also shown are the areas covered by the JADES NIRCam fields (*bracketed by the orange lines*). The coordinates of $z \sim 8$–9 and $z \sim 10$–13 candidate galaxies in our selection are indicated by the red and dark red circles, respectively. The four white stars indicate the coordinates for the four $z \sim 10$–14 galaxies which have been spectroscopically confirmed by the JADES NIRSpec observations in Curtis-Lake et al. (2022) and Robertson et al. (2022).

two-colour Lyman-break criteria have been shown to largely have the redshifts that were targeted by the selection (e.g. Steidel et al. 1999, 2003; Stark et al. 2010; Ono et al. 2012; Finkelstein et al. 2013; Oesch et al. 2015, 2016; Zitrin et al. 2015; Hashimoto et al. 2018; Jiang et al. 2021), and so it makes sense to continue using those criteria for even higher redshift selections with *JWST*.
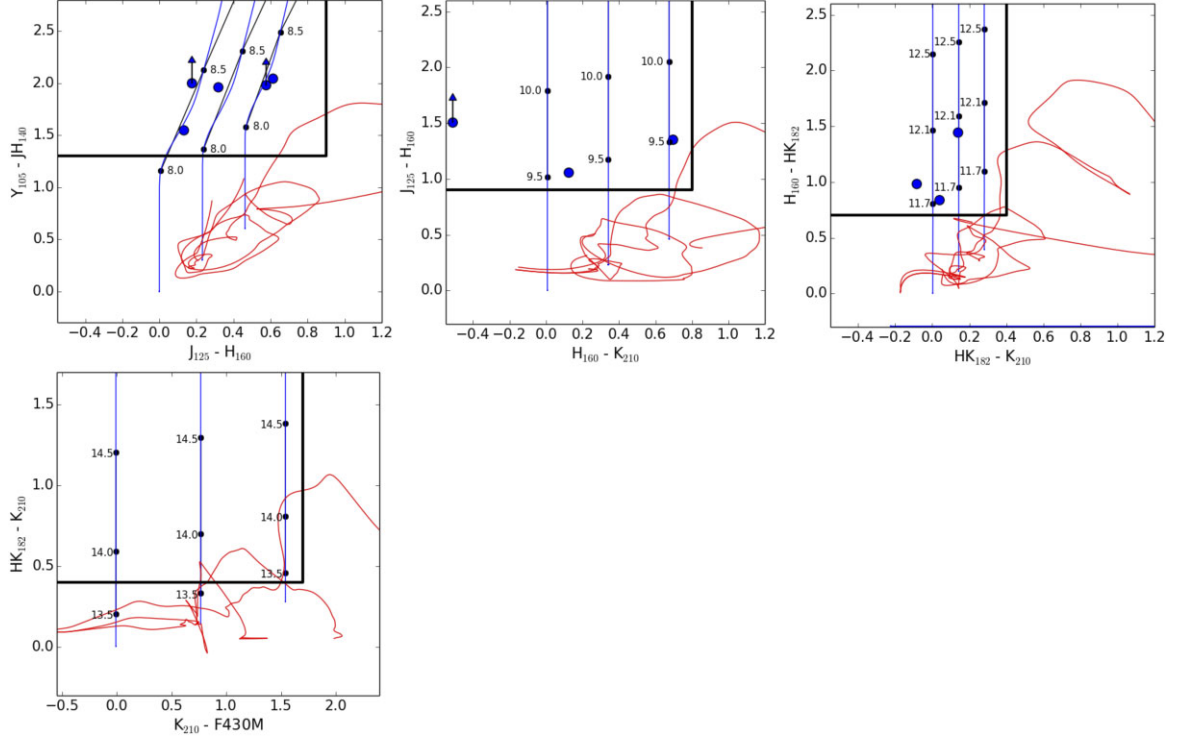
Figure 3. Illustration of the main colour criteria we use to identify galaxies at $z \sim 8$–9 (upper left), $z \sim 10$–11 (up per center), $z \sim 12$–13 (upper right), and $z \sim 14$–15 (lower left). The thick black lines indicate the boundaries of our primary colour–colour criteria (but note that for our $z \sim 8$–9 selection we also include sources with J_{125}–H_{160} colours redder than 0.3 mag and Y_{105}–JH_{140} colours redder than 0.8). The blue lines indicate the expected colours of star-forming galaxies with 100 Myr constant star-formation histories and $E(B - V)$ dust extinction of 0, 0.15, and 0.3, with colours at specific redshifts indicated by the black dots. The red lines show the expected colours of lower-redshift template galaxies from Coleman, Wu & Weedman ([1980]) out to $z \sim 7$. The solid blue circles show the colours of specific sources in our selection. In cases where sources are not detected in a band, they are shown with an arrow at the 1σ limit.

In detail, we adopt the following two colour criteria:

$$((Y_{105} - JH_{140} > 1.3) \vee$$
$$((Y_{105} - JH_{140} > 0.8) \wedge (J_{125} - H_{160} > 0.3))) \wedge$$
$$(J_{125} - H_{160} < 0.9)$$

for our $z \sim 8$–9 selection,

$$(J_{125} - H_{160} > 0.9) \wedge (H_{160} - HK_{182} < 0.8) \wedge$$
$$(H_{160} - K_{210} < 0.8)$$

for our $z \sim 10$–11 selection,

$$(H_{160} - HK_{182} > 0.7) \wedge (HK_{182} - K_{210} < 0.4)$$

for our $z \sim 12$–13 selection, and

$$(HK_{182} - K_{210} > 0.4) \wedge (K_{210} - F430M < 1.7)$$

for our $z \sim 14$–15 selection. In applying the above colour criteria, sources which are undetected in a band are set to their 1σ upper limits. These colour criteria are illustrated in Fig. 3 relative to the expected colours of star-forming galaxies at $z > 7$ and various low-redshift interlopers.

To exclude lower-redshift interlopers, we coadd the flux from the imaging observations blueward of the Lyman break using the χ^2 statistic (Bouwens et al. [2011b]), which we define as $\chi^2 = \Sigma_i \mathrm{SGN}(f_i)(f_i/\sigma_i)^2$ where f_i is the flux in band i in a consistent aperture, σ_i is the uncertainty in this flux, and $\mathrm{SGN}(f_i)$ is equal to 1 if $f_i > 0$ and -1 if $f_i < 0$. Sources which show $\chi^2 > 9$ coadding the flux in the $B_{435}V_{606}i_{775}I_{814}z_{850}$, $B_{435}V_{606}i_{775}I_{814}z_{850}Y_{105}$, $B_{435}V_{606}i_{775}I_{814}z_{850}Y_{105}J_{125}$, and

$B_{435}V_{606}i_{775}I_{814}z_{850}Y_{105}J_{125}JH_{140}H_{160}$ bands in our $z \sim 8$–9, $z \sim 10$–11, $z \sim 12$–13, and $z \sim 14$–15 selections, respectively, are excluded due to their possibly being lower redshift interlopers. We impose this criterion in three apertures, i.e. a 0.2 arcsec diameter aperture, a 0.35 arcsec diameter aperture, and the small scalable Kron apertures we use to make colour measurements. Additionally, we exclude any $z \gtrsim 10$ sources which show a 3σ detection in the Y_{105} band due to this band's providing the most sensitive imaging at >1 μm, which nevertheless probes blueward of the Lyman break.

To ensure that the sources we detect are real, sources are required to show a 5σ detection in the combined F182M + F210M image in a 0.35 arcsec diameter aperture, to show a 3σ detection in the F182M and F210M image individually in a 0.35 arcsec diameter aperture, to show a 4σ detection in the combined F182M + F210M image in a 0.2 arcsec diameter aperture. Sources in our $z \sim 10$–11 selection are required to show a 3σ detection in either the F140W + F160W image or the F160W image.

Following our selection of candidate $z \sim 8$–13 sources based on the described two colour criteria, we computed redshift likelihood functions $P(z)$ for each source using the EAZY photometric redshift code (Brammer, van Dokkum & Coppi [2008]). In fitting the photometry of individual sources, we made use of spectral templates from the EAZY_v1.0 set and Galaxy Evolutionary Synthesis Models (GALEV; Kotulla et al. [2009]), which includes nebular continuum and emission lines according to the prescription provided in Anders & Fritze-v. Alvensleben ([2003]), a 0.2 $Z_\odot$ metallicity, and scaled to a rest-frame EW for Hα of 1300 Å. >80 per cent of the integrated redshift likelihood, i.e. $P(z > 5.5) > 0.8$, is required to be at $z > 5.5$ for sources to be retained in our $z \geq 8$ selections.
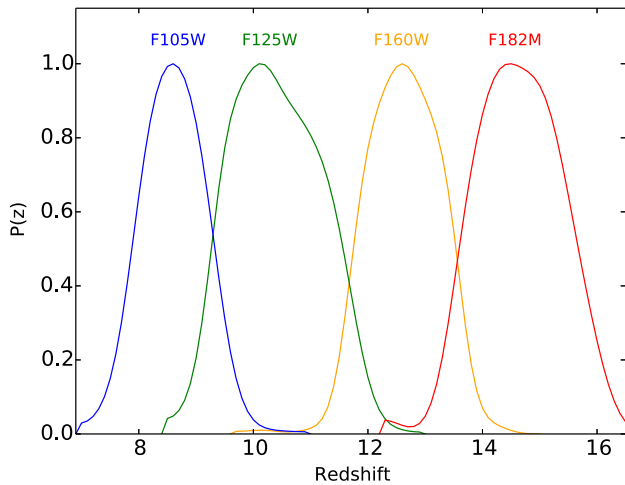
Figure 4. Redshift selection functions for our $z \sim 8$–9 Y_{105}-dropout, $z \sim 10$–11 J_{125}-dropout, $z \sim 12$–13 H_{160}-dropout, and $z \sim 14$–15 HK_{182}-dropout selections. The criteria for these selections is described in Section 3.1. The expected redshift distribution of these selections is estimated using our selection volume simulations in Section 4.1 and has a mean value of 8.7, 10.5, 12.6, and 14.7, respectively.

All candidate $z \geq 8$ galaxies are then subjected to a visual inspection and any sources that correspond to apparent diffraction spikes or due to an artificially high background in a region of the image are excluded by hand.

Finally, to investigate whether our selection might be contaminated by lower-mass stars, we examined the SEXTRACTOR STELLARITY parameter derived in the HK_{182} and K_{210} bands for all of the sources which satisfied our other selection criteria. Given the narrow PSF in the HK_{182} and K_{210} bands, with an effective FWHM of 0.06–0.07 arcsec, these data provide us with the best constraints on whether sources are point-like. Of the sources still remaining in our selection, XDFJ-2381146246 and XDFY-2394748078 are the most consistent with being point-like, with STELLARITY parameters in excess of 0.8 in one or both the HK_{182} and K_{210} bands. Comparing the χ^2 of SED fits to these sources with SED fits to lower mass stars from the SpeX library (Burgasser 2014),[2] we find significantly better fits ($\Delta\chi^2 > 4$) to high-redshift star-forming templates from EAzY than to the lower-mass star templates.

The approximate redshift selection windows for our three $z \geq 8$ selections over the HUDF are shown in Fig. 4 and are estimated based on the selection volume simulations described in Section 4.1.

3.2 Selection results

In total, we identify five sources satisfying our $z \sim 8$–9 selection criteria, three sources satisfying our $z \sim 10$–11 criteria, two sources satisfying our $z \sim 12$–13 criteria, and 0 sources satisfying our $z \sim 14$–15 criteria. The results of our selection are summarized in Table 2.

Remarkably, the brightest source is in our $z \sim 12$–13 selection, and it was previously identified in the available *HST* data over the HUDF as UDFj-39546284 (Bouwens et al. 2011a). While the initial redshift estimate was $z \sim 10.3$ based on data from the HUDF09 program (Bouwens et al. 2011b), the non-detection of the source in the JH_{140} band from the HUDF12 program (Ellis et al. 2013) resulted in the

[2]http://pono.ucsd.edu/~adam/browndwarfs/spexprism/index.html

photometric redshift estimate increasing to $z = 11.9 \pm 0.1$ (Bouwens et al. 2013; Ellis et al. 2013; McLure et al. 2013; Oesch et al. 2013). Given the implied luminosity of the source and very high redshift, an alternate interpretation of the source was that it was an extreme emission line candidate at $z \sim 2$ (Bouwens et al. 2013; Brammer et al. 2013; Ellis et al. 2013). Brammer et al. (2013) even presented evidence for a tentative 2.7σ line detection at ~ 1.6 μm based on the available WFC3/IR grism data over the HUDF.

Thanks to the availability of very deep NIRCam observations over the HUDF, we can determine that the galaxy is actually at $z \sim 12$ based on the detection of a flat *UV*-continuum redward of the apparent Lyman break and possible Balmer break at ~ 4.8 μm (Fig. 5). Our confidence in this conclusion is substantially bolstered by the exceptional sensitivity of the archival optical + near-IR observations in multiple passbands blueward of the break. The source UDFj-39546284 appears to have been the most distant galaxy detected with *HST* during its more than 30 yr of operation.

Parallel spectroscopy of XDFH-239446286 by the JADES GTO team with NIRSpec find strong evidence for a sharp spectral break in the source at ~ 1.53 μm, demonstrating that the source is at 11.58 ± 0.05 (Curtis-Lake et al. 2022; Robertson et al. 2022), lower than our photometric redshift estimate of $z \sim 12$ but consistent within 2σ.

The best-fitting SEDs for the three sources in our $z \sim 10$–11 sample and the second source in our $z \sim 12$–13 sample are presented in Fig. 6. Postage stamps of the sources in our $z \sim 12$–13 and $z \sim 10$–11 samples are presented in Figs 7 and 8. Similar to XDFH-239446286, spectroscopy by the JADES GTO team confirm a second source from our selection XDFJ-2381146246 as lying at $10.38^{+0.07}_{-0.06}$, within 1σ of our photometric redshift estimate.

Postage stamps and SEDs for the five sources which make it into our $z \sim 8$–9 selection are presented in Figs A1 and A2 of Appendix A. Interestingly enough, two of the sources XDFY-2381345542 and XDFY-2394748078 show evidence for very high EW [O III] + Hβ line emission based on the prominent detections in both the F460M and F480M bands. The contribution of the emission lines to both bands indicate that the lines likely lie in the overlap region between the two medium bands, allowing us to obtain very precise constraints on their photometric redshifts from the photometry to $z = 8.5 \pm 0.1$. The impact that strong [O III] + Hβ line emission can have in improving photometric redshift constraints recalls similar improvements made to $z \sim 7$ sources leveraging *Spitzer*/IRAC photometry (Smit et al. 2014, 2015; Zitrin et al. 2015; Roberts-Borsani et al. 2016; Bouwens et al. 2022b). While it may seem fortuitous to find two galaxies from our selection in such a small redshift interval, the presence of one galaxy in that interval makes the occurence of another more likely. We will discuss this further in Section 4.3.

We also estimated photometric redshifts with PROSPECTOR (Johnson et al. 2021), adopting a flat redshift prior $0 < z_{phot} < 12$. PROSPECTOR runs on the FLEXIBLE STELLAR POPULATION SYNTHESIS (FSPS) package (Conroy & Wechsler 2009; Conroy & Gunn 2010) with the MODULES FOR EXPERIMENTS IN STELLAR ASTROPHYSICS ISOCHRONES AND STELLAR TRACKS (MIST; Choi et al. 2016; Dotter 2016). For these measurements, we adopted a constant star-formation history (CSFH), a Chabrier (2003) IMF defined between 0.1 and 240 M$_\odot$, a Calzetti et al. (2000) extinction curve, a $Z_{star} \equiv Z_{gas} = 0.2$ Z$_\odot$ metallicity, and a ionization parameter log $U = -2.5$ (e.g. Stark et al. 2017; De Barros et al. 2019). We also adopted the nebular emission (both continuum and lines) estimates that natively come with the FSPS package (Byler et al. 2017), obtained by reprocessing the FSPS templates through CLOUDY (Ferland et al. 2013). We refer the reader

Table 2. Selection of $z \geq 8$ Galaxies by leveraging new *JWST*/NIRCAM medium band data over the HUDF/XDF.

ID	RA	DEC	z^a_{phot} EAzY	Prosp	M_{UV} [mag][b]	m_{UV} [mag][b]	Lyman Break [mag][c]	$\Delta\chi^{2a, d}$	p(z>5.5)[a]	Lit[1]
					$z \sim 8$–9 selection					
XDFY-2376346017	03:32:37.64	−27:46:01.7	$8.3^{+0.2}_{-0.2}$	$7.9^{+0.1}_{-0.1}$	-19.3 ± 0.1	28.0 ± 0.1	1.4 ± 0.2	-45.0	1.000	M13,B15
XDFY-2381345542	03:32:38.13	−27:45:54.2	8.5 ± 0.1	$8.4^{+0.1}_{-0.0}$	-19.6 ± 0.1	27.7 ± 0.1	1.9 ± 0.3	-79.5	1.000	B11,M13,O13,B15
XDFY-2394748078	03:32:39.47	−27:48:07.9	8.5 ± 0.1	$8.4^{+0.1}_{-0.0}$	-18.8 ± 0.1	28.5 ± 0.1	1.5 ± 0.8	-35.3	1.000	E13,M13,O13
XDFY-2392146324	03:32:39.21	−27:46:32.5	$8.6^{+0.3}_{-0.3}$	$8.2^{+1.1}_{-0.3}$	-18.1 ± 0.2	29.2 ± 0.2	>1.9	-15.9	1.000	E13,M13,O13,B15
XDFY-2426447051	03:32:42.64	−27:47:05.1	$8.8^{+0.4}_{-0.3}$	$8.7^{+0.4}_{-0.3}$	-18.4 ± 0.2	28.9 ± 0.2	>1.4	-9.9	0.994	E13,M13,O13
					$z \sim 10$–11 selection					
XDFJ-2402448006	03:32:40.24	−27:48:00.6	$9.2^{+0.6}_{-0.6}$	$9.1^{+0.5}_{-0.4}$	-17.9 ± 0.6	29.7 ± 0.6	>1.0	-3.7	0.907	O13,B15
XDFJ-2381146246[e]	03:32:38.12	−27:46:24.6	$9.8^{+0.6}_{-0.6}$	$9.7^{+0.4}_{-0.4}$	-18.1 ± 0.4	29.5 ± 0.4	>1.7	-5.3	0.957	B11,O13,B15
XDFJ-2404647339	03:32:40.47	−27:47:33.9	$11.4^{+0.4}_{-0.5}$	$10.8^{+0.6}_{-0.6}$	-18.6 ± 0.2	28.9 ± 0.2	>1.5	-10.0	0.993	–
					$z \sim 12$–13 selection					
XDFH-2334046578	03:32:33.41	−27:46:57.8	$11.8^{+0.4}_{-0.6}$	$11.9^{+0.5}_{-0.6}$	-18.6 ± 0.2	29.2 ± 0.2	1.0 ± 0.4	-17.3	1.000	–
XDFH-2395446286[f]	03:32:39.55	−27:46:28.67	$12.0^{+0.1}_{-0.2}$	$11.9^{+0.1}_{-0.1}$	-20.0 ± 0.1	27.8 ± 0.1	1.0 ± 0.1	-61.1	1.000	B11,E13,M13,O13, B13

[1] B11 = Bouwens et al. (2011a), E13 = Ellis et al. (2013), M13 = McLure et al. (2013), O13 = Oesch et al. (2013), B15 = Bouwens et al. (2015a)
[a] Derived using EAzY (Brammer et al. 2008) and Prospector (Johnson et al. 2021)
[b] Derived using the flux in the H_{160}, HK_{182}, and K_{210} bands for sources in our $z \sim 8$–9, $z \sim 10$–11, and $z \sim 12$–13 samples to probe the *UV* luminosity at ≈ 1600 Å rest-frame.
[c] Amplitude of the nominal Lyman breaks for these $z \geq 8$ galaxy candidates.
[d] $\chi^2_{best,z>5.5} - \chi^2_{best,z<5.5}$
[e] $z_{\mathbf{NIRSpec}} = \mathbf{10.38^{+0.07}_{-0.06}}$ (Curtis-Lake et al. 2022; Robertson et al. 2022)
[f] $z_{\mathbf{NIRSpec}} = 11.58 \pm 0.05$ (Curtis-Lake et al. 2022; Robertson et al. 2022)
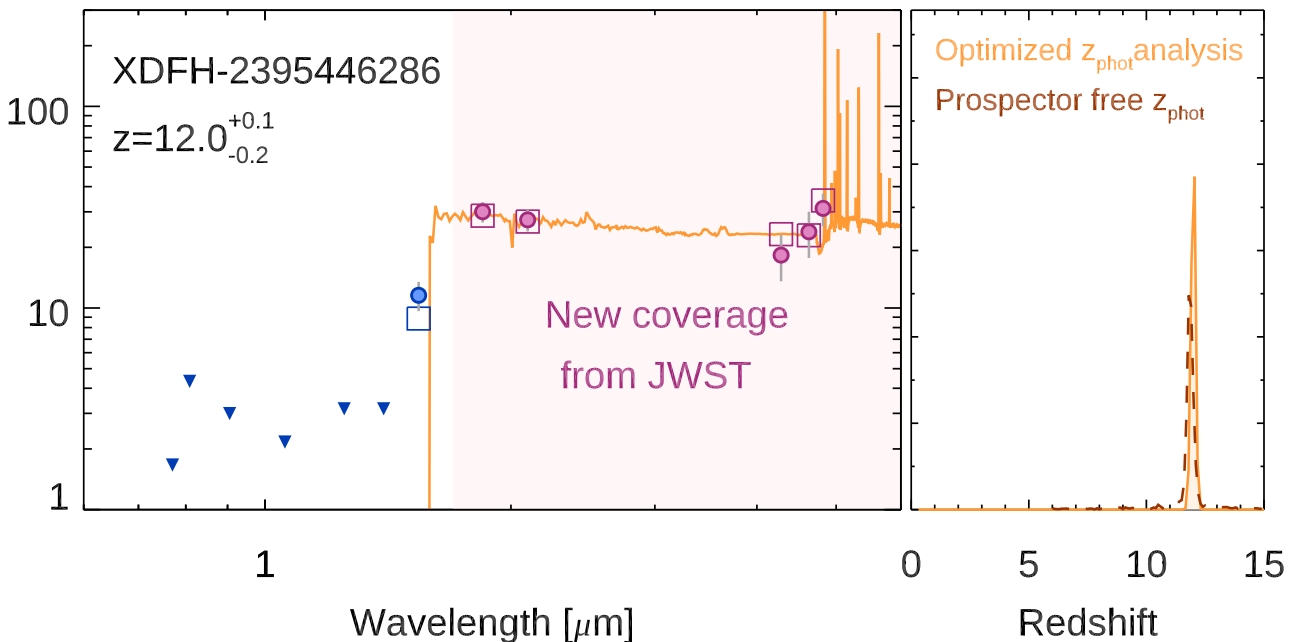

Figure 5. (*left*) Fits of a model spectral energy distribution to the observed *HST* + *JWST* photometry available for the highest redshift candidate UDFj-39546284 identified over the HUDF with *HST* (Bouwens et al. 2011a). Flux measurements blueward of 1.6 μm are with *HST* (*blue filled points and downward triangles*) and those redward of this limit are with *JWST* (*magenta filled points*). The blue downward triangles correspond to 2σ upper limits on the fluxes. The open squares indicate the expected fluxes from the best-fitting SED model. (*right*) Redshift likelihood distribution derived for UDFj-39546284 from the EAzY photometric redshift code (Brammer et al. 2008) on our photometric measurements, and UDFj-39546284 seems to almost certainly have a redshift of $z = 12.0^{+0.1}_{-0.2}$, as the JADES team has confirmed with spectroscopy (Curtis-Lake et al. 2022) and similar to what Ellis et al. (2013), McLure et al. (2013), Oesch et al. (2013), and Bouwens et al. (2013) inferred using the available *HST* + *Spitzer* data in 2013. As such, UDFj-39546284 appears to be the most distant galaxy discovered by *HST* in its more than 30 yr of operation. Fig. 7 shows postage stamp images of this source.
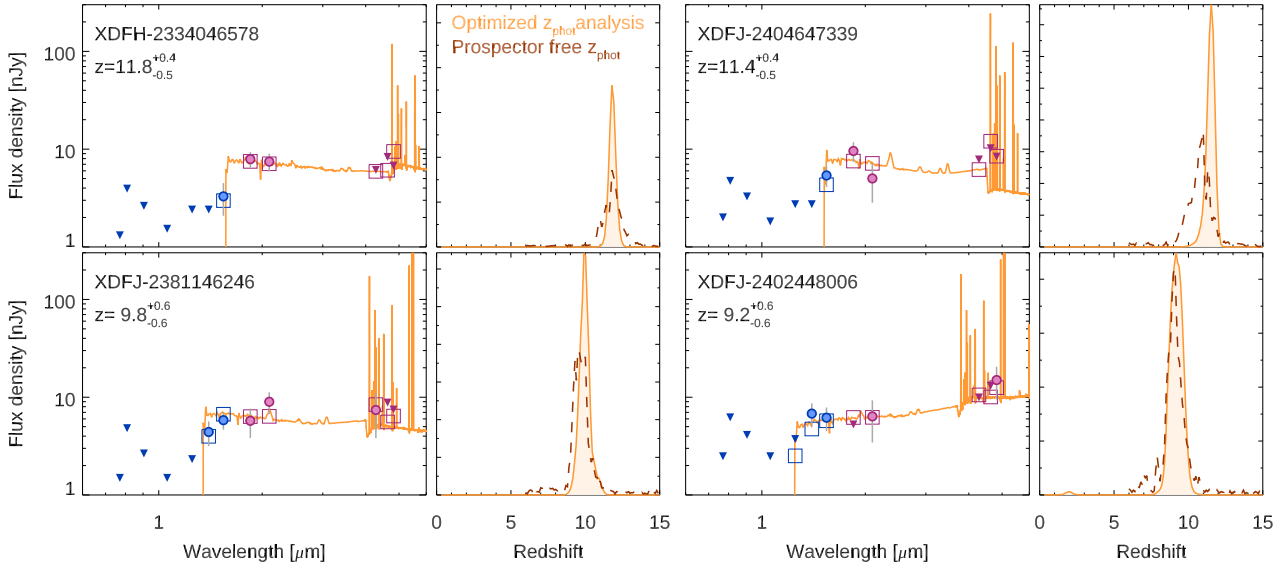
Figure 6. Similar to Fig. 5 but for the four high redshift candidates in our $z \sim 10$–11 and $z \sim 12$–13 samples. In all four cases, the likelihood that the candidates are at very high redshift, i.e. $z > 5.5$, is >90 per cent. XDFJ-2381146246 has now been spectroscopically confirmed to have a redshift of $10.38^{+0.07}_{-0.06}$ by the JADES team (Curtis-Lake et al. 2022).
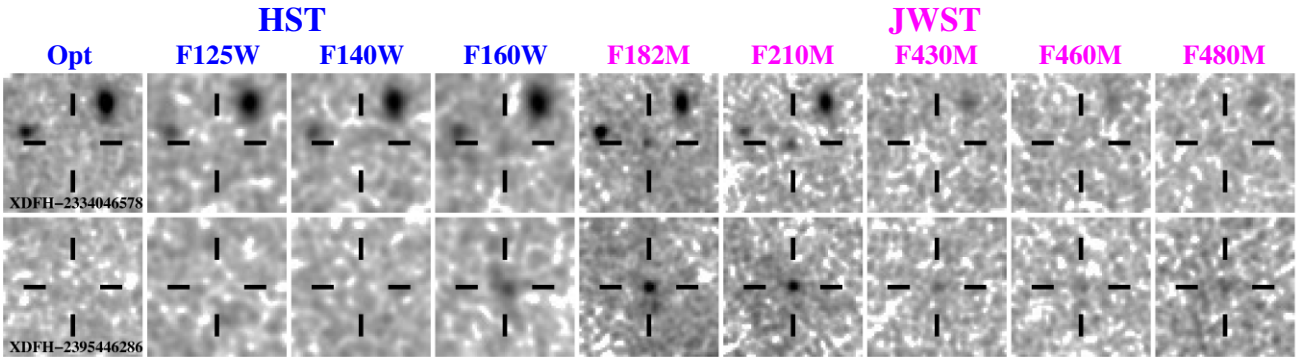

Figure 7. Postage stamp images (2.4 arcsec × 2.4 arcsec) of the two $z \sim 12$ galaxy candidates we identified over the HUDF using the new *JWST* medium band F182M, F210M, F430M, F460M, and F480M data and archival *HST* XDF observations in the F125W, F140W, and F160W bands. The 'Opt' column shows a stack of the observations in the *HST* F435W, F606W, F775W, F814W, F850LP, and F105W bands. Both candidates show $\geq 4\sigma$ detections in both the F182M and F210M bands, but no detection in the F140W band or any bluer band. XDFH-2395446286 is detected at even higher significance ($\geq 7.5\sigma$) in the F182M and F210M bands, while also being well detected ($\gtrsim 4\sigma$) in the redder F430M, F460M, F480M medium bands. XDFH-2395446286 was first identified by Bouwens et al. (2011a) as a probable $z \geq 10$ galaxy and then later argued to lie at $z \sim 12$ because of the source's showing no detection in the F140W band observations (Bouwens et al. 2013; Ellis et al. 2013; McLure et al. 2013; Oesch et al. 2013) obtained by the HUDF12 program (Ellis et al. 2013).

to Byler et al. (2017) for full details on the adopted procedure and for a detailed characterization of the results.

The agreement between the Prospector and EAzY results were excellent, being within one sigma in all cases except one where the difference was less than 2σ. This agreement gives some confidence that our photometric redshifts are fairly robust.[3]

---

[3]Strong emission lines can significantly contribute to the flux density in those photometric bands which intercept their emission. Because this potentially introduces complementary constraints to the photometric redshift measurements, we note that the templates corresponding to ages of 3, 30, and 300 Myr have rest-frame equivalent widths EW_0 for $[O\,2]_{\lambda 3727}$ of $EW_0([O\,2]_{\lambda 3727}) \sim 510$, 170, and 110 Å respectively, $EW_0(H\beta) \sim 590$, 170, 80 Å, $EW_0([O\,3]_{\lambda 4959}) \sim 890$, 120, 110 Å, and $EW_0([O\,3]_{\lambda 5007}) \sim 2700$, 690, 330 Å.

All five of the sources in our $z \sim 10$–11 and $z \sim 12$–13 samples appear to be very reliable, with $P(z > 5.5) > 0.9$ for all sources in the selection and with 8 of the 10 showing $P(z > 5.5) > 0.99$. This constitutes a significantly higher fraction of reliable sources than we find (Bouwens et al. 2022a) for the majority of the $z > 8$ candidates reported over the SMACS0723 (Pontoppidan et al. 2022), GLASS NIRCam parallel field (Treu et al. 2022), and the first four pointings from CEERS. The higher reliability of the present selection of $z > 8$ galaxies appears to be a consequence of the sensitivity of the archival observations from *HST* over the field (≥ 30.0 mag at 5σ from ~ 0.4 to 0.8 μm), being up to ~ 2 mag deeper at optical wavelengths than observations over CEERS, SMACS0723, or the GLASS parallel.

We note the presence of a third possible $z \sim 12$–13 candidate at 03:32:37.25, -27:46:01.9 that missed our selection due to the detection of this source at 3σ in the Y_{105} band in a 0.35 arcsec diameter aperture. While it is unclear how reliable that candidate is based
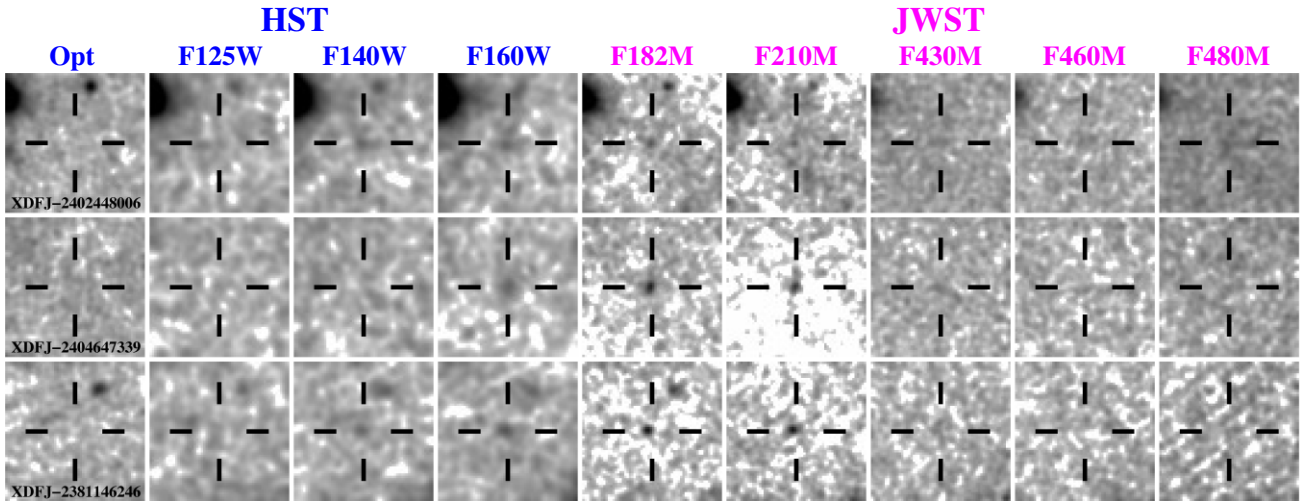
Figure 8. Similar to Fig. 7 but for the three $z \sim 10$–11 galaxies in our selection. XDFJ-2381146246 was first identified as a candidate $z \sim 10$ galaxy by Bouwens et al. (2011a) and later confirmed as a strong candidate by Oesch et al. (2013) and Bouwens et al. (2015a). XDFJ-2402448006 was first identified by Oesch et al. (2013) and again identified by Bouwens et al. (2015a). XDFJ-2404647339 is identified for the first time as a candidate $z \sim 10$–11 galaxy here.

on archival imaging observations with *HST*, this should be easily clarified using the very sensitive F115W observations the NIRCam GTO team is obtaining as part of the JADES programme (Bunker, NIRSPEC Instrument Science Team & JADES Collaboration 2020; Robertson 2022).

3.3 Comparison with earlier selections with the *Hubble Space Telescope* and new spectroscopic sample from JADES

Previously, Bouwens et al. (2011b, 2013, 2015a), Ellis et al. (2013), McLure et al. (2013), and Oesch et al. (2013), considered searches for $z \geq 8.5$ galaxies over the HUDF. Of the sixteen unique $z \gtrsim 8.5$ candidate galaxies reported as part of these analyses, our selection recovers eight.

The remaining eight candidates do not satisfy our selection criteria and there are a variety of reasons for this, which we detail in Appendix B, but here we provide a brief summary. For five of the candidates, this is due to these candidates' failing to show 2σ detections in the new medium-band F182M and F210M imaging observations with NIRCam. For another candidate (C5 from Appendix B), this is because the source is detected at $>5\sigma$ significance in the Y_{105} band. For another candidate (C7 from Appendix B), this is because the source was not identified in the SEXTRACTOR catalog we constructed over the HUDF. Finally, for the final remaining candidate (C6 from Appendix B), this is because the integrated likelihood at $z > 5.5$ does not exceed the 80 per cent threshold required to be part of our $z \geq 8$ selection (Section 3.1).

In parallel with the photometric identifcation of high-redshift candidates conducted as part of our analysis, the JADES team also was considering potential photometric candidate z>10 galaxies around the HUDF. NIRSpec follow-up observations conducted by the JADES succeeded in confirming four of these candidates, finding redshifts of $10.38^{+0.07}_{-0.06}$, $11.58^{+0.05}_{-0.05}$, $12.63^{+0.24}_{-0.08}$, and $13.20^{+0.04}_{-0.07}$. Of the four sources, three lie inside the 4.6 arcmin^2 search field we consider while one lies outside the region. Of the three sources in our search field, two are found in our photometric sample. The other does not appear in our selection since it does not satisfy our H_{160}-dropout selection criteria, due to its only showing a modest spectral break (~ 0.4 mag) across the H_{160} and HK_{182} bands.

4 RESULTS

4.1 Luminosity function estimates

The optical plus near-IR observations from HST over the HUDF and similarly deep medium-band NIRCam imaging data from JWST's JEMS together constitute a very deep data set that provides stronger constraints to the blue of the Lyman-alpha break than many of the data sets that have been available from the early JWST observations, allowing us to identify some of the highest-quality high-redshift candidates known to date. This arguably puts us in position to obtain some of the most reliable *UV* LF results to date in the early universe.

Given the small number of sources available over the HUDF, we derive maximum likelihood results on the *UV* LF at $z > 8$ adopting Poissonian statistics. As in our own earlier analyses, we derive LF results by maximizing the likelihood $\mathcal{L}$ of producing the observed distribution of apparent magnitudes given some model LF,

$$\mathcal{L} = \Pi_i \, p(m_i) \tag{1}$$

where the likelihood of a specific LF is computed over a set of apparent magnitude intervals m_i. Since Poissonian statistics are assumed, the probability of finding $n_{\mathrm{observed},\,i}$ sources

$$p(m_i) = e^{-n_{\mathrm{expected},i}} \frac{(n_{\mathrm{expected},i})^{n_{\mathrm{observed},i}}}{(n_{\mathrm{observed},i})!} \tag{2}$$

where $n_{\mathrm{observed},\,i}$ is the number of sources observed in a given magnitude interval i while $n_{\mathrm{expected},\,i}$ is the expected number using some model LF. The number of expected sources $n_{\mathrm{expected},\,i}$ is computed based on some model LF ϕ_j from the equation

$$n_{\mathrm{expected},i} = \Sigma_j \phi_j V_{i,j} \tag{3}$$

where $V_{i,j}$ is the effective volume over which a source in the magnitude interval j can be both selected and have a measured magnitude in the interval i.

Selection volumes are computed for our four samples by inserting artificial sources with various redshift and apparent magnitudes at random positions within the NIRCam images and then attempting both to detect the sources and to select them using our $z \sim 8$–9, $z \sim 10$–11, $z \sim 12$–13, and $z \sim 14$–15 criteria. We assume point-source sizes for the galaxies we add to various images and assume the *UV*-

Table 3. Binned LF results for Galaxies at $z \geq 8$.

M_{UV}	ϕ^* [mag^{-1} Mpc^{-3}]
z ~ 8–9 galaxies	
−20.02	0.000166 ± 0.000132
−18.77	0.000252 ± 0.000250
z ~ 10–11 galaxies	
−18.90	0.000086 ± 0.000120
−17.90	0.000746 ± 0.000738
z ~ 12–13 galaxies	
−20.06	0.000078 ± 0.000062
−18.81	0.000190 ± 0.000152

continuum slopes of sources to have a mean value of −2.3, with a 1σ scatter of 0.4. The present size assumptions are not especially different from that found for galaxies at $z \sim 8$–17, both using earlier HST observations (Coe et al. 2013; Zitrin et al. 2014; Lam et al. 2019) and now using *JWST* observations (Naidu et al. 2023, 2022; Ono et al. 2022). These *UV*-continuum slopes are in reasonable agreement with determinations available on the basis of both *HST* + *Spitzer* data (e.g. Dunlop et al. 2013; Bouwens et al. 2014a; Wilkins et al. 2016; Stefanon et al. 2022a) and now *JWST* data (Cullen et al. 2023; Topping et al. 2022a).

We computed selection volumes of ~1750, ~2500, ~1500, and ~1500 cMpc^3 per arcmin^2 at brighter *UV* luminosities for our $z \sim$ 8–9, $z \sim$ 10–11, $z \sim$ 12–13, and $z \sim$ 14–15 samples, respectively, corresponding to Δz redshift slices of 1.1, 1.7, 1.0, and 1.0, respectively. At fainter *UV* luminosities near the limit of our selection, i.e. −19 to −18 mag, we estimated selection volumes of ~1600, ~2300, ~870, and ~30 cMpc^3 per arcmin^2. While the correction factors can become quite large for faint sources in our highest-redshift selection, no sources are identified in those selections, so it only has a minimal impact on our LF results.

Recomputing selection volumes by applying the Ono et al. (2022) $(1 + z)^{-1.2}$ size scaling to the $z \sim 4$ galaxy population from the HUDF (Bouwens et al. 2015a), we estimate selection volumes just 10 per cent lower than what we estimate adopting point-source sizes. This indicates that the uncertain sizes of higher redshift galaxies are unlikely to have affected our results in any significant way. Furthermore, it suggests it is improbable that there are many extended sources at $z > 8$ that have evaded our selections due to their large sizes.

We derive determinations of the *UV* LF results in 0.5-mag bins and determinations of the best-fitting Schechter function. For the Schechter function results, we fix the M^* to −21.15 mag consistent with the $z \geq 7$ *UV* LF derived by Bouwens et al. (2021), while we fix α to −2.26, −2.38, −2.71, and −2.93 at $z \sim$ 8–9, $z \sim$ 10–11, $z \sim$ 12–13, and $z \sim$ 14–15 consistent with an extrapolation of the LF fit results of Bouwens et al. (2021) to the respective redshifts.

We present our binned *UV* LF results at $z \sim$ 8–9, $z \sim$ 10–11, and $z \sim$ 12–13 LF results in both Table 3 and Fig. 9. The parameterized fit results are presented in Table 4 and shown in Fig. 9 as the red lines. Encouragingly enough, our new LF results at $z \sim$ 8–9 are consistent with what we obtained from our earlier analyses leveraging a comprehensive set of HST fields (Bouwens et al. 2021). Agreement with earlier results is not especially surprising given the significant overlap between the present selection and earlier selections.

At $z \sim 10.5$, our results are consistent with what we previously obtained in Bouwens et al. (2015a) and Oesch et al. (2018). This is not especially surprising since both of these previous studies made use of the $z \sim 10$ searches over the HUDF/XDF to constrain the

faint end of the *UV* LF and we use the same volume here, albeit with slightly better sampling of the volume just above $z \sim 10$.

At $z \sim 12.6$, our new LF results appear to be ~3-4× higher than found in the analyses of Donnan et al. (2023), Harikane et al. (2023), and Finkelstein et al. (2022b), but consistent with what Naidu et al. (2023) find. The substantially higher normalization of our $z \sim$ 12–13 LF results follows from our discovery of two $z \sim$ 12–13 candidates over the relatively small-area 4.6 arcmin^2 HUDF. The HUDF covers a ~10× smaller area than used in other contemporary studies with *JWST*, e.g. Donnan et al. (2023), Harikane et al. (2023), and Finkelstein et al. (2022b). As a result, one could imagine that our results are subject to a larger large scale structure uncertainty than results obtained over wider areas, but the following estimate suggests that uncertainty is nevertheless modest. Using the Trenti & Stiavelli (2008) cosmic variance calculator,[4] we estimate a ~52 per cent RMS uncertainty in the normalization of our *UV* LF results at $z \sim 12.6$ from cosmic variance which is smaller than the uncertainties from small number statistics.

4.2 Determinations of the star formation rate density

With new determinations of the *UV* LF leveraging the extremely deep *JWST* + *HST* imaging observations over the HUDF, we are in position to reexamine the evolution of the *UV* luminosity density from early times. When compared to other concurrent analyses of JWST observations, results derived over the HUDF have the advantage of being more robust against contamination from lower redshift sources, but have the disadvantage of relying on a very small volume, resulting in a larger uncertainty from cosmic variance.

We derive our constraints on the evolution of the *UV* luminosity density by directly integrating our stepwise *UV* LF results to −18 mag – given that this is the luminosity to which solid constraints exist. We do not consider results fainter than this to avoid extrapolating the results beyond where we can directly measure them from the observations.

We present our results in Table 5 and in Fig. 10. We convert these results to a SFR density using the conversion factor $\mathcal{K}_{\mathcal{FUV}}$ is $0.7 \times 10^{-28} \mathrm{M_\odot}$ year^{-1} erg^{-1} s Hz from Madau & Dickinson (2014), which assumes a Chabrier (2003) IMF, a constant star formation rate, and metallicity $Z = 0.002 \, \mathrm{Z_\odot}$. To ensure that the results from Oesch et al. (2018), Bouwens et al. (2021), Donnan et al. (2023), and Harikane et al. (2023) are presented to a similar limiting luminosity, we have made a correction to several of new luminosity density results from *JWST* before presenting them in Fig. 10. The correction was made by integrating the fiducial LFs from each of these studies down to both −18 mag (the limit we use) and −17 mag (the limit to which many results were quoted in the original studies) and then correcting results based on the difference.

To place the new results in context, we compare them to the results of four different theoretical models which assume a constant star formation efficiency. These include Mason et al. (2015), Tacchella et al. (2018), Bouwens et al. (2021), and Harikane et al. (2022). Results from these models are shown on Fig. 10 using the orange solid, orange dot–dashed, orange dotted, and orange dashed lines, respectively.

Similar to other early studies of the evolution of the *UV* LF from $z \sim 15$ (e.g. Donnan et al. 2023; Harikane et al. 2023), the present results lie above the predictions of the constant star formation efficiency models, suggesting that either star formation
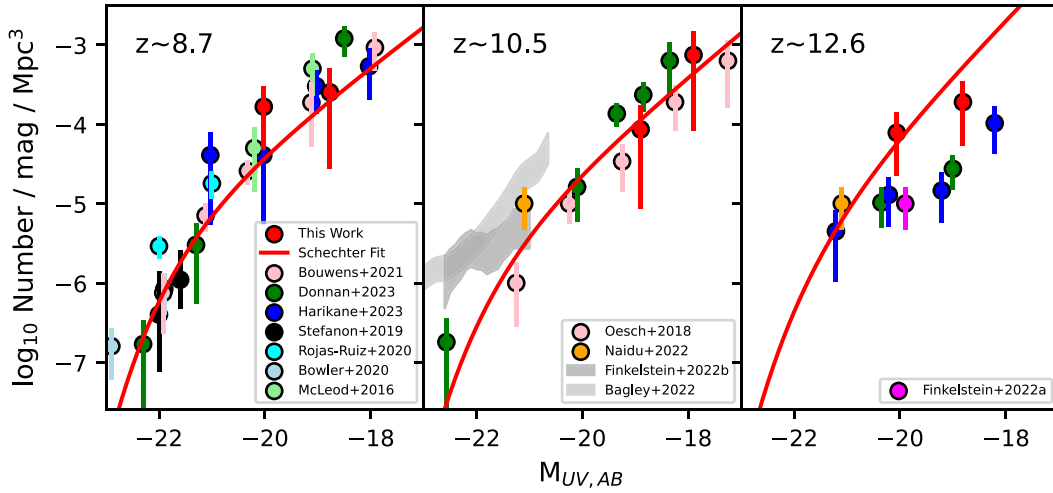
---

[4] https://www.ph.unimelb.edu.au/cgi-bin/mtrenti/prova.cgi

Figure 9. Present determinations of the stepwise and Schechter *UV* LF results at $z \sim 8–9$, $z \sim 10–11$, and $z \sim 12–13$ (*red circles* and *red lines*, respectively) using the $z \geq 9$ candidate galaxies we have identified in the combined *HST + JWST* data set over HUDF. Also shown are the LF results from Bouwens et al. (2021; pink circles), Donnan et al. (2023; green circles), Harikane et al. (2023; blue circles), Stefanon et al. (2019; black circles), Rojas-Ruiz et al. (2020; cyan circles), Bowler et al. (2020; light blue circles), McLeod, McLure & Dunlop (2016; light green circles), Oesch et al. (2018; pink circles), Finkelstein et al. (2022b; dark grey-shaded region), Bagley et al. (2022; light grey-shaded region), Naidu et al. (2023; orange circles), and Finkelstein et al. (2022a; magenta circles). Several other determinations of the *UV* LF at $z \geq 9$ (McLure et al. 2013; Oesch et al. 2013, 2014; Bouwens et al. 2014b; Calvi et al. 2016; Bouwens et al. 2016a; Ishigaki et al. 2018; Livermore et al. 2018; Morishita et al. 2018; Bhatawdekar et al. 2019; Bouwens et al. 2019; Morishita 2021; Leethochawalit et al. 2022; which have been important historically) are not shown, but provide similar constraints to the others presented. Our new LF results at $z \sim 9–10$ are fairly similar to earlier work with *HST* and *JWST*. While our $z \sim 12–13$ LF estimates are higher than other recent determinations with *JWST*, we emphasize that the uncertainties in our results are large, being based on only two sources identified within a small volume.

Table 4. Best-fitting parameters derived for Schechter fits to the present $z \geq 8$ *UV* LF results.

Redshift	ϕ^* [10^{-5} mag^{-1} Mpc^{-3}]	M^* [mag]	α
		Schechter	
8.7	$1.5^{+1.0}_{-0.6}$	-21.15 (fixed)	-2.26 (fixed)
10.5	$0.8^{+0.8}_{-0.4}$	-21.15 (fixed)	-2.38 (fixed)
12.6	$1.6^{+2.0}_{-1.0}$	-21.15 (fixed)	-2.71 (fixed)
14.7	$<2.7^a$	-21.15 (fixed)	-2.93 (fixed)

[a] Upper limit is 1σ.

Table 5. Inferred *UV* luminosity densities[1] in the early Universe derived from the $z \geq 8$ search over the HUDF/XDF.

Redshift	ρ_{UV} [erg s^{-1} Mpc^{-3}]	ρ_{SFR} [M$_\odot$ yr^{-1} Mpc^{-3}]
8.7	25.15 ± 0.24	-3.00 ± 0.24
10.5	24.33 ± 0.30	-3.82 ± 0.30
12.6	$24.91^{+0.37}_{-0.48}$	$-3.24^{+0.37}_{-0.48}$
14.7	$<25.56^a$	$<-2.59^a$

[1] Luminosity densities integrated down to -18 mag.
[a] Upper limit is 1σ.

in the earliest generation of galaxies is either substantially more efficient than at later times, shows a significantly greater deviation relative to the mean main-sequence evolution for galaxies (Mason, Trenti & Treu 2023), or the mass-to-light ratio of stars is much lower, possibly indicative of significantly modified IMF (Inayoshi

et al. 2022; Harikane et al. 2023; Steinhardt et al. 2022), or a number of other explanations (e.g. Ferrara, Pallottini & Dayal 2022; Harikane et al. 2023; Kannan et al. 2022; Mirocha & Furlanetto 2023).

While each of these possibilities would be exciting, it is clear that further study, including validation and investigation of these results with spectroscopy from *JWST*, and theoretical modeling (e.g. Boylan-Kolchin 2022; Kannan et al. 2022; Lovell et al. 2023; Mason et al. 2023; Mirocha & Furlanetto 2023; Wilkins et al. 2023) will be required to ascertain what is driving the presence of so many luminous galaxies in the early universe.

4.3 Stellar population analysis

Thanks to the depth of the *JWST* NIRCam observations at $\geq 2~\mu$m and medium band coverage which allow for a probe of the EW of emission lines like [O III] $+ H\beta$, we can place much tighter constraints on the stellar population parameters of the faint $z \geq 8$ galaxies identified within the HUDF than was possible with *HST* [see also Whitler et al. (2023a), Leethochawalit et al. (2023), Furtak et al. (2023), Bradley et al. (2022), and Endsley et al. (2022)].

Table 6 summarizes the main stellar population parameters of our sample. These were estimated using the Bayesian tool PROSPECTOR (Johnson et al. 2021), which runs on the FLEXIBLE STELLAR POPULATION SYNTHESIS (FSPS) package (Conroy & Wechsler 2009; Conroy & Gunn 2010) with the MODULES FOR EXPERIMENTS IN STELLAR ASTROPHYSICS ISOCHRONES AND STELLAR TRACKS (MIST; Choi et al. 2016; Dotter 2016). For our measurements, we adopted a Chabrier (2003) IMF defined between 0.1 and 240 M$_\odot$, a Calzetti et al. (2000) extinction curve, a $Z_{star} \equiv Z_{gas} = 0.2~Z_\odot$ metallicity, a ionization parameter $\log U = -2.5$ (e.g. Stark et al. 2017; De Barros et al. 2019), and a formation redshift of $z = 20$ (Hashimoto et al. 2018; Mawatari et al. 2020; Harikane et al. 2022; Tacchella et al. 2022). We also adopted the nebular emission (both
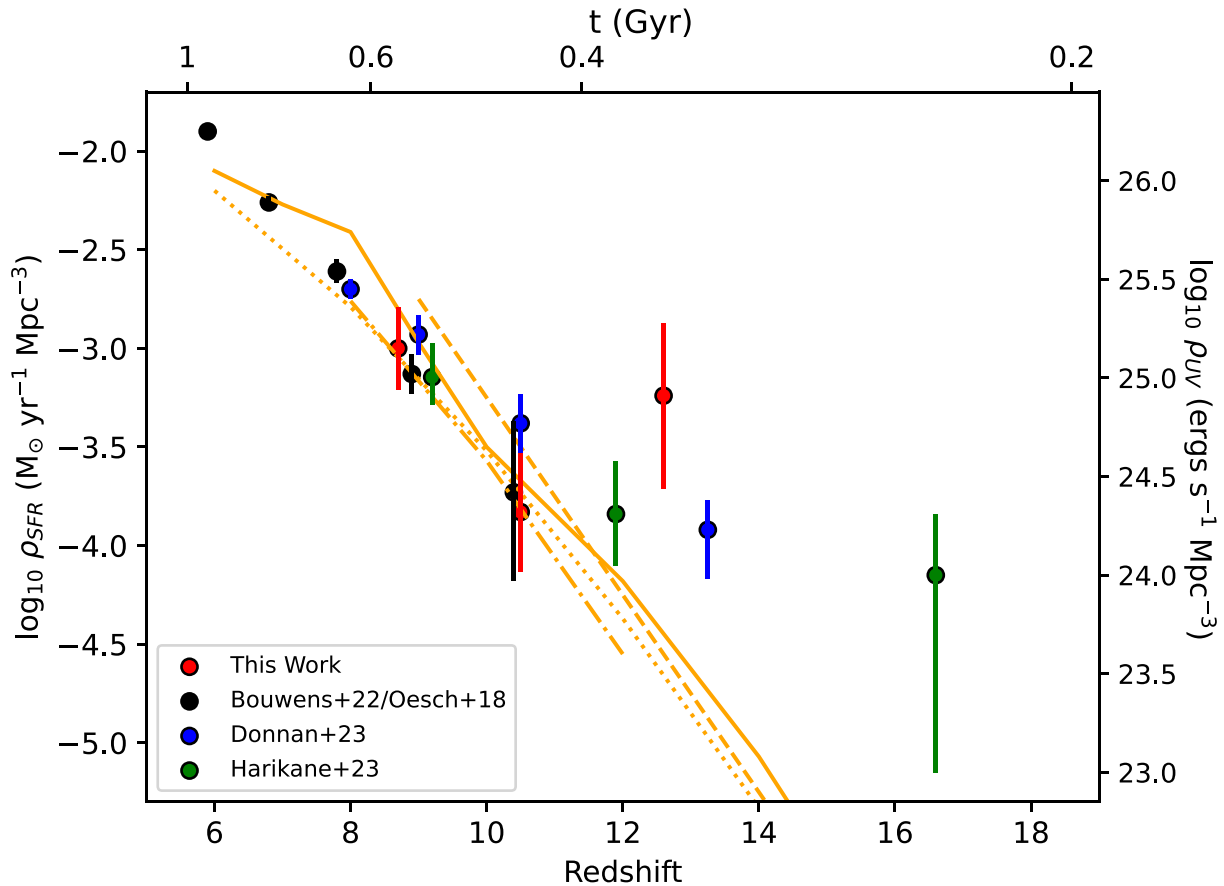
Figure 10. *UV* luminosity and star formation rate density integrated to −18 mag. Shown are determinations from the present analysis (*red circles*), Donnan et al. (2023; *blue circles*), Harikane et al. (2022; *green circles*), and Bouwens et al. (2021)/Oesch et al. (2018; *black circles*). The orange lines indicate the expected evolution in the *UV* luminosity density assuming no evolution in the star formation efficiency of galaxies across cosmic time using the models of Mason, Trenti & Treu (2015; solid), Tacchella et al. (2018; dot–dashed), Bouwens et al. (2021; dotted), and Harikane et al. (2022; dashed). The present determination of both the *UV* luminosity and SFR density at $z \sim 12$–13 is substantially higher than both other LF results in the literature, but is good agreement with earlier results at lower redshifts. It is unclear why the *UV* luminosity densities we derive at $z \sim 12$ are so much higher than other results, but we emphasize the present estimate is very uncertain, being based on just two sources identified within a small volume. Whatever the case, the present LF results suggest that the *UV* luminosity and SFR density may undergo a much milder evolution from early times than expected in many theoretical models.

continuum and lines) estimates that natively come with the FSPS package (Byler et al. 2017), obtained by reprocessing the FSPS templates through CLOUDY (Ferland et al. 2013). We refer the reader to Byler et al. (2017) for full details on the adopted procedure and for a detailed characterization of the results.

Our estimates are based on a non-parametric SFH (e.g. Leja et al. 2019b; Topping et al. 2022b; Whitler et al. 2023b), defined over four bins in time measured backwards from the cosmic time corresponding to the redshift of each source. Specifically, the four bins were fixed at 0–3, 3–13, 13–100, and 100–300 Myr, respectively, with a Student's t-distribution continuity prior modulating the ratio of the SFR in contiguous bins, with $\nu = 2$ and $\sigma = 2$ (see Stefanon et al. 2022b, and discussions in Leja et al. 2019a; Tacchella et al. 2022). This configuration can concurrently accommodate a recent burst of star formation and significant star formation during the initial assembly of the galaxy (Hashimoto et al. 2018; Roberts-Borsani, Ellis & Laporte 2020; Tacchella et al. 2022; Whitler et al. 2023b). We note here that previous tests with up to 8 bins in time (0–3, 3–13, 13–100 Myr, and log-spaced afterwards) found marginal differences in the final parameter estimates (e.g. Stefanon et al. 2022b). This is

indeed reassuring, given the coarse spectral resolution provided by the currently available photometry can pose severe challenges to any attempts of constraining the SFH of individual sources.

We present two distinct SFR measurements. One (SFR_{100}) is obtained by averaging the total mass formed in the last 100 Myr as estimated through the template analysis with PROSPECTOR, while the other (SFR_{UV}) is computed by converting the UV luminosity using the factors listed by Madau & Dickinson (2014), interpolated for a $Z = 0.2 \, Z_\odot$ metallicity, a Chabrier (2003) IMF, and adopting a negligible dust emission, as recent results at high redshifts suggest (e.g. Bouwens et al. 2016b, 2020; Dunlop et al. 2017; McLure et al. 2018), and consistent with the small A_V values obtained with the non-parametric analysis. We finally computed sSFR ($\equiv SFR/M_\star$) combining the SFR_{100} and $M_\star$ values previously estimated.

We computed UV slopes β following the procedure of Stefanon et al. (2019). Briefly, we constructed a grid of UV slope values based on stellar population models from the Bruzual & Charlot (2003) template set and attenuation $A_V = 0$–3 mag. We then fit the corresponding synthetic flux densities in the bands blue-ward of the rest-frame 2800 Å to the observations. We computed uncertainties

Table 6. Main stellar population parameters for our sample.

ID	$z_{\rm phot}^{a}$	UV slope β^{b}	SFR_{UV}^{c} [M$_\odot$ yr^{-1}]	SFR_{100}^{d} [M$_\odot$ yr^{-1}]	$\log_{10}(M_\star/M_\odot)^{e}$	sSFR^{f} [Gyr^{-1}]	$\log_{10}(t_{50}/{\rm yr})^{g}$	$\log_{10}(t_{80}/{\rm yr})^{g}$	A_V [mag]	EW ([O III] + Hβ)^{h} [Å]
					$z \sim 12$–13 selection					
XDFH-2395446286	$12.0^{+0.1}_{-0.2}$	$-2.8^{+1.1}_{-0.4}$	$3.1^{+0.6}_{-0.5}$	$3.3^{+3.0}_{-2.2}$	$8.7^{+0.3}_{-0.5}**$	$9.9^{+19.5}_{-7.0}**$	$7.83^{+0.07}_{-0.08}**$	$7.99^{+0.14}_{-0.05}**$	$0.08^{+0.09}_{-0.05}$	$\ldots\,\dagger$
XDFH-2334046578	$11.8^{+0.4}_{-0.5}$	$-2.6^{+1.8}_{-0.6}$	$0.8^{+0.3}_{-0.2}$	$1.0^{+1.3}_{-0.7}$	$8.0^{+0.4}_{-0.6}**$	$17.5^{+59.9}_{-14.8}**$	$7.81^{+0.11}_{-0.13}**$	$8.01^{+0.16}_{-0.07}**$	$0.10^{+0.12}_{-0.07}$	$\ldots\,\dagger$
					$z \sim 10$–11 selection					
XDFJ-2404647339	$11.4^{+0.4}_{-0.5}$	$-3.2^{+0.8}_{-0.0}$	$0.7^{+0.2}_{-0.1}$	$0.9^{+1.5}_{-0.4}$	$7.9^{+0.5}_{-0.4}$	$24.1^{+86.4}_{-19.1}$	$7.86^{+0.19}_{-0.17}$	$8.15^{+0.10}_{-0.19}$	$0.18^{+0.22}_{-0.12}$	$\ldots\,\dagger$
XDFJ-2381146246	$9.8^{+0.6}_{-0.6}$	$-1.6^{+0.9}_{-0.9}$	$0.5^{+0.1}_{-0.1}$	$1.0^{+2.1}_{-0.6}$	$7.4^{+0.5}_{-0.4}$	$55.7^{+124.7}_{-41.4}$	$7.49^{+0.41}_{-0.48}$	$8.16^{+0.13}_{-0.28}$	$0.26^{+0.27}_{-0.17}$	$\ldots\,\dagger$
XDFJ-2402448006	$9.2^{+0.6}_{-0.6}$	$-2.6^{+1.3}_{-0.6}$	$0.5^{+0.1}_{-0.1}$	$1.6^{+2.5}_{-1.1}$	$8.2^{+0.4}_{-0.6}$	$19.0^{+54.5}_{-14.6}$	$7.98^{+0.25}_{-0.23}$	$8.36^{+0.08}_{-0.31}$	$0.62^{+0.40}_{-0.36}$	$\ldots\,\dagger$
					$z \sim 8$–9 selection					
XDFY-2426447051	$8.8^{+0.4}_{-0.3}$	$-2.9^{+0.9}_{-0.2}$	$0.6^{+0.1}_{-0.1}$	$1.3^{+1.9}_{-0.9}$	$7.9^{+0.4}_{-0.5}$	$28.9^{+79.9}_{-22.8}$	$7.74^{+0.16}_{-0.27}$	$8.07^{+0.27}_{-0.16}$	$0.08^{+0.09}_{-0.05}$	317 ± 139
XDFY-2392146324	$8.6^{+0.3}_{-0.4}$	$-3.2^{+1.0}_{-0.0}$	$0.4^{+0.1}_{-0.1}$	$0.7^{+1.0}_{-0.5}$	$7.7^{+0.4}_{-0.6}$	$25.0^{+80.6}_{-20.3}$	$7.77^{+0.14}_{-0.21}$	$8.04^{+0.31}_{-0.12}$	$0.07^{+0.08}_{-0.05}$	<396
XDFY-2381345542	$8.5^{+0.1}_{-0.1}$	$-2.8^{+0.4}_{-0.4}$	$1.6^{+0.2}_{-0.2}$	$1.7^{+0.4}_{-0.4}$	$7.4^{+0.1}_{-0.1}$	$75.8^{+18.3}_{-15.3}$	$2.29^{+0.96}_{-1.25}$	$5.99^{+0.27}_{-0.36}$	$0.01^{+0.01}_{-0.01}$	2313 ± 275
XDFY-2394748078	$8.5^{+0.1}_{-0.1}$	$-1.8^{+0.4}_{-0.4}$	$0.8^{+0.1}_{-0.1}$	$1.2^{+1.8}_{-0.6}$	$7.3^{+0.4}_{-0.3}$	$76.8^{+118.7}_{-49.9}$	$6.64^{+0.76}_{-1.42}$	$8.05^{+0.25}_{-0.54}$	$0.14^{+0.14}_{-0.09}$	2260 ± 269
XDFY-2376346017	$8.3^{+0.2}_{-0.2}$	$-2.7^{+0.4}_{-0.4}$	$1.4^{+0.2}_{-0.2}$	$1.1^{+0.6}_{-0.7}$	$8.3^{+0.2}_{-0.4}$	$6.9^{+9.3}_{-4.3}$	$7.80^{+0.04}_{-0.06}$	$7.96^{+0.02}_{-0.02}$	$0.03^{+0.04}_{-0.02}$	$\ldots\,*$
Median		-2.7	0.7	1.1	7.9	24.5	7.80	8.04	0.09	1288

^{a}From EAzY (Brammer et al. 2008)

^{b}UV slope, computed from the photometry in the bands probing rest-frame wavelengths between 1700 Å and 2800 Å.

^{c}Unobscured SFR measured from the rest-frame UV luminosity, following the relation of Madau & Dickinson (2014) for a $Z = 0.2\,Z_\odot$ metallicity.

^{d}Average SFR in over the last 100 Myr inferred from the total mass in stars formed over the last 100 Myr estimated by PROSPECTOR adopting the non-parametric SFH.

^{e}Mass in surviving stars. This was obtained by multiplying the total mass formed since the onset of star formation by the fraction of surviving stars estimated by PROSPECTOR adopting the non-parametric SFH.

^{f}Specific star-formation rate, computed as the ratio between SFR$_{100}$ and $M_\star$.

^{g}Lookback time, in logarithmic units, required to form the second half (t_{50}) and the last 80 per cent (t_{80}) of the stellar mass, inferred from the non-parametric SFH.

^{h}Cumulative equivalent width of Hβ and [O III]$_{\lambda\lambda 4959,\,5007}$ emission lines, measured on the best-fitting SED template. Values in parenthesis mark those measurements extracted for sources lacking photometric coverage in the bands where the Hβ and [O III]$_{\lambda\lambda 4959,\,5007}$ line emissions is expected at the nominal redshift of the specific source.

$\dagger$The available photometry does not provide coverage at wavelengths expected for Hβ and [O III] line emission.

$\ddagger$These measurements correspond to the photometric 2σ upper limits in the F480W band.

$*$The continuum estimated by the SED fit is brighter than the 2σ upper limits in the bands where the Hβ and [O III]$_{\lambda\lambda 4959,\,5007}$ line emissions is expected at the nominal redshift of the specific source.

$**$These estimates exclusively rely on rest-UV light and are therefore potentially much more uncertain.

by randomly perturbing the observed flux densities and refitting. This procedure allows us to make full use of the near-IR data and to naturally take into account redshift uncertainties.

Remarkably, the observations in the medium bands provided by JEMS program (Williams et al. 2023) not only enable pinpointing the photometric redshifts for three sources in our sample. The $\sim 3\sigma$–10σ detections in the NIRCam/F460M and F480M also allow for accurate estimates of the intensity of the Hβ and [O III]$_{\lambda\lambda 4959,\,5007}$ lines for redshifts $z \sim 8.5$. We measured the equivalent widths (EW) of these lines from the ratio between the flux density in the F480M band and the continuum inferred from the best-fitting SED template, given the current lack of $>2\sigma$ detection in bands probing the continuum free from emission lines in our sample. Uncertainties in the EW were computed by randomly perturbing the flux densities according to the corresponding 1σ uncertainties 1000 times, and repeating the measurement following our main procedure. We finally verified that our EW measurements were consistent at $\leq 1\sigma$ with the cumulative EW(Hβ+ [O III]) measured on the best-fitting SED templates.

Overall, we find markedly blue UV slopes (median $\beta_{\rm med} \sim -2.7$), elevated sSFR (sSFR$_{\rm med} \sim 24.5$ Gyr^{-1}) and extreme nebular line emission (EW$_{\rm med}$([O III] + Hβ) ~ 1300 Å), suggesting very young stellar populations. Specifically, our UV slopes measurements are consistent with recent results at similar redshifts based on JWST

data (e.g. Bradley et al. 2022; Whitler et al. 2023a), and consistent although marginally bluer than the measurements of Cullen et al. (2023).

Perhaps unsurprisingly, the typical stellar masses characterizing our sample lie in range $\log M_\star/M_\odot \sim 7.3$–$8.7$, populating the low-mass end of the stellar mass function at these redshifts (e.g. Stefanon et al. 2022a). The associated sSFR range between sSFR~ 7–80 Gyr^{-1}, consistent with recent measurements (e.g. Bradley et al. 2022), and implying mass assembly time-scales of $\lesssim 10$–100 Myr (for a constant SFH). Such rapid assemblies are also qualitatively supported by the typical formation times as estimated through the non-parametric SFH (t_{50} and t_{80} in Table 6).

Our sSFR measurements are presented in Fig. 12, together with previous estimates at $z \sim 8$ by Stefanon et al. (2022a), at $z \sim 10$ by Stefanon et al. (2023), and a compilation of measurements including Labbé et al. (2013), Duncan et al. (2014), Smit et al. (2014), Salmon et al. (2015), Faisst et al. (2016), Mármol-Queraltó et al. (2016), Santini et al. (2017), Davidzon et al. (2018), Khusanova et al. (2020), Strait et al. (2020), Endsley et al. (2021), Roberts-Borsani et al. (2022), Tacchella et al. (2022), Topping et al. (2022b), and Bradley et al. (2022). Our new estimates push current constraints on the sSFR to $z \sim 12$ (although the stellar masses $M_\star$ of $z > 10$ galaxies in our selection only have weak constraints on their rest-frame optical
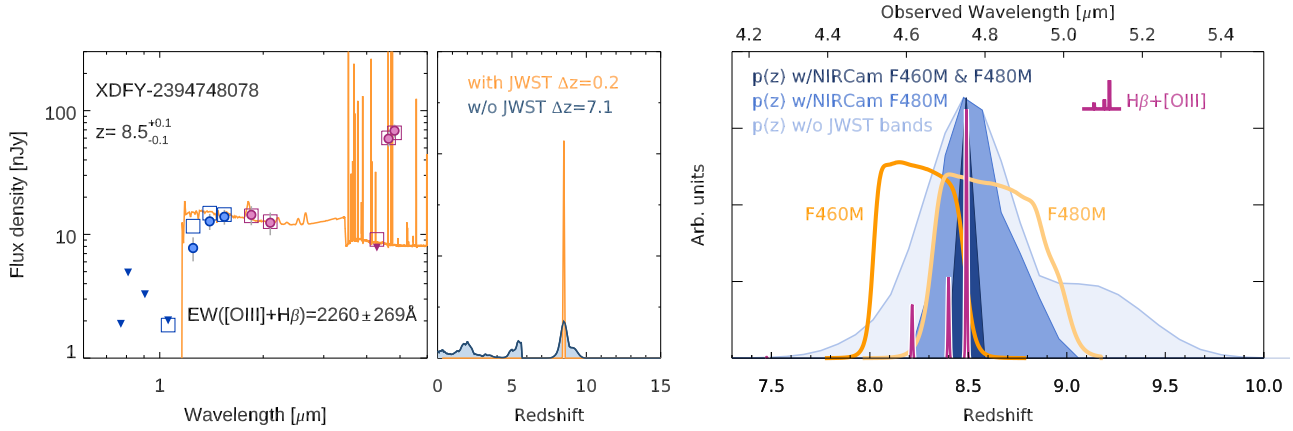
Figure 11. (*left*) Similar to Fig. 5 but for one $z \sim 8$–9 galaxy candidate appearing to contain prominent emission from the [O III] +Hβ lines in the F460M + F480M medium band filters demonstrating the dramatic impact the new JWST medium band observations have in improving the photometric redshift constraints on this candidate. (*right*) Illustration of the extremely precise constraints one can derive on the photometric redshift of sources when a prominent set of emission lines lie in the overlap region between two medium band filters F460M and F480M (whose sensitivity is shown with the orange lines). Thanks to the prominent line emission in both bands, we can constrain the photometric redshifts of XDFY-2394748078 to $z = 8.5 \pm 0.1$, which is much more precise than most of our other photometric redshift estimates and similar to the constraints we could obtain if these emission lines fell within one of NIRCam's narrow bands. In addition, the medium band observations allow us to constrain the EWs [O III] + Hβ lines to 2260 $\pm$ 269Å.
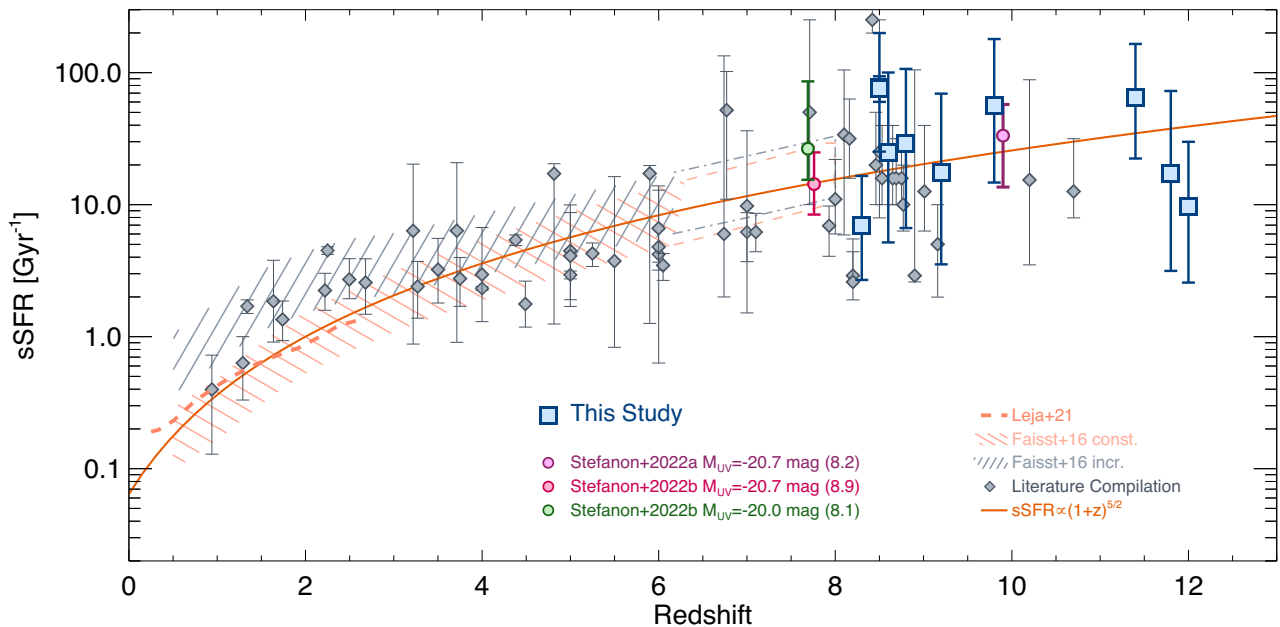
Figure 12. Inferred sSFRs for faint $z \geq 8$ galaxies identified over the HUDF/XDF (filled blue squares), and comparison to the evolution of the sSFR to lower redshift. The lower redshift estimates include the results of Faisst et al. (2016), Leja et al. (2022), and Stefanon et al. (2023, 2022a), and a compilation (solid grey diamonds) with the measurements from Labbé et al. (2013), Duncan et al. (2014), Smit et al. (2014), Salmon et al. (2015), Mármol-Queraltó et al. (2016), Santini et al. (2017), Davidzon et al. (2018), Khusanova et al. (2020), Strait et al. (2020), Endsley et al. (2021), Roberts-Borsani et al. (2022), Tacchella et al. (2022), Topping et al. (2022b), and Bradley et al. (2022). The orange solid curve corresponds to the model of Dekel et al. (2013), which star formation is taken to be the direct result of the inflow of cold gas driven by the hierarchical assembly of the dark matter halos, and is modulated by a non-evolving efficiency of star formation. Our new measurements extend constraints on the evolution of the sSFR to $z \sim 12$. Importantly, the results seem to remain consistent with the toy model of Dekel et al. (2013), suggesting that a marginally evolving star-formation efficiency is plausible starting as early as just $\sim$370 Myr after the Big Bang.

light from the F480M flux measurements); moreover, comparison with previous estimates further supports a scenario where the sSFR monotonically increases with increasing redshift (see e.g. Stefanon et al. 2023, 2022a) up to $z \sim 12$.

To put these new results in context, in Fig. 12 we compare the compilation of sSFR estimates with the predictions of the model by Dekel et al. (2013). These predictions were obtained from analytical

considerations on the Extended Press-Schechter formalism (see also Neistein & Dekel 2008; Weinmann, Neistein & Dekel 2011; Genel et al. 2014), and assuming a non-evolving conversion factor between the specific accretion rate of the dark matter halos and the sSFR. The remarkable agreement between measurements out to $z \sim 12$ and the model suggests a marginally evolving star formation efficiency out to just $\sim$370 Myr into cosmic time.

Finally, the accurate EW measurements enabled by the NIRCam medium-band filters reveal extreme [O III] + Hβ line emission, ∼1.5 × more intense than previous estimates based on *Spitzer*/IRAC colours (e.g. Stefanon et al. 2022a), and further support the scenario that galaxies with very intense radiation fields are ubiquitous in the early Universe (e.g. Schaerer et al. 2022).

5 SUMMARY

Here we have taken advantage of sensitive medium-band observations acquired over the *Hubble* Ultra Deep Field from the JEMS program (Williams et al. 2023) to extend searches for star-forming galaxies there to even higher redshift, i.e. $z > 10$, than was possible with the *Hubble* Space Telescope. The medium band observations are a good match to the depth of the *HST* observations but probe redward to 2.1 μm in the short wavelength channel, allowing for sensitive searches for galaxies to $z \sim 15$.

Searches for $z \geq 8$ star-forming galaxies over the *Hubble* Ultra Deep Field have the important advantage of having the most sensitive available supporting observations with *HST*, resulting in the most reliable selections of $z \geq 8$ galaxies for which spectroscopy is not yet available.

Using the combined *HST* + *JWST* data set, we construct sensitive photometric catalogs of all the sources over the *Hubble* Ultra Deep Field and employ a two-colour Lyman-break selection to search for star-forming galaxies at $z \sim 8$–9, $z \sim 10$–11, $z \sim 12$–13, and $z \sim 14$–15. The mean redshift estimated for these selections using selection volume simulations is 8.7, 10.5, 12.6, and 14.7, respectively.

Interestingly enough, based on these selections, we find that the highest redshift candidate source identified in *HST* data, i.e. UDFj-39546284 (Bouwens et al. 2011a), does in fact have a redshift of $z = 12.0^{+0.1}_{-0.2}$, as suggested by analyses by Ellis et al. (2013), McLure et al. (2013), Oesch et al. (2013), and Bouwens et al. (2013). Parallel spectroscopy from the JADES team (Curtis-Lake et al. 2022; Robertson et al. 2022) find that the source has a spectroscopic redshift of 11.58 ± 0.05. The source is thus the most distant galaxy identified by *HST* in its more than 30 yr of operation. It is not an extreme emission line source as had been alternatively suggested earlier by Ellis et al. (2013), Bouwens et al. (2013), and Brammer et al. (2013).

Besides this $z \sim 12$ source, we find 5, 3, 1, and 0 additional galaxies in our $z \sim 8$–9, $z \sim 10$–11, $z \sim 12$–13, and $z \sim 14$–15 selections, two of which are entirely new discoveries from the *JWST* data. The photometric redshifts of the new sources are $z \sim 11$ and $z \sim 12$, which is in excess of what is easily identified in the available *HST* data over the HUDF/XDF.

Leveraging these new selections, we run selection volume simulations and compute *UV* LF results at $z \sim 8.7$, $z \sim 10.5$, $z \sim 12.6$, and $z \sim 14.7$ (Section 4.1). At $z \sim 8.7$ and $z \sim 10.5$, our results are consistent with earlier HUDF results at these redshifts. However, at $z \sim 12.6$, we infer a 5–10× higher normalization for the *UV* LF than for contemporary analyses in the literature and more consistent with results at $z \sim 8$–9.

Given the limited volume and the presence of only two sources in our $z \sim 12.6$ selection, our *UV* LF results at $z \sim 12.6$ are accordingly very uncertain. Nevertheless, like other early results on the *UV* LF evolution with *JWST* from $z \sim 15$, our results lie substantially in excess of the predictions of constant star formation efficiency models that are effective in modeling the evolution of *UV* LF and galaxy properties for much of cosmic time (Mason et al. 2015; Tacchella et al. 2018; Bouwens et al. 2021; Harikane et al. 2022). It is unclear what this means, but could mean that star formation is substantially more efficient than at later times, the evolution of the main sequence

of star formation in galaxies shows a much greater variation relative to the mean (Mason et al. 2023), or the mass-to-light ratio of star formation (and hence the IMF) is substantially shifted relative to later times (Harikane et al. 2023; Steinhardt et al. 2022).

We also made use of the NIRCam imaging redward of 2 μm to characterize the stellar populations of the sources and rest-frame EWs of [O III] + Hβ (Section 4.3). Based on our analysis, we find that the typical star-forming galaxy in our sample had a very blue *UV*-continuum slope $\beta \sim -2.7$, an elevated sSFR ~ 24.5 Gyr^{-1}, while showing extremely high-EW line emission in [O III] + Hβ with a median EW of ∼1300 Å.

We note that while our $z \sim 12.6$ *UV* LF results are in excess of what one might predict for constant star formation efficiency models, the evolution we find for the sSFRs of galaxies from $z \sim 12$ is nonetheless in better agreement (Fig. 12). While it is unclear what would resolve these tensions, perhaps the small HUDF volume shows a particular overdensity of $z \sim 12$ sources or there is an evolution in the IMF from high-redshift as speculated in multiple studies (e.g. Inayoshi et al. 2022; Harikane et al. 2023; Steinhardt et al. 2022). Clearly, this is an issue that will need to be investigated further in future data sets.

The presence of extreme line emission from [O III] + Hβ (EWs of ∼2300 Å) is particularly convincing in the cases of XDFY-2381345542 and XDFY-2394748078 due to the substantial flux excesses seen in the F460M and F480M medium bands (Fig. A1) over that seen in the F430M band. The present inferences regarding the stellar populations of $z \sim 8$–13 galaxies extend the trend in galaxy properties seen from lower redshifts to $z \geq 8$ with *HST* + *Spitzer* (Stefanon et al. 2022a) and also with *JWST* (Bradley et al. 2022; Cullen et al. 2023; Endsley et al. 2022; Furtak et al. 2023; Leethochawalit et al. 2023; Topping et al. 2022a).

In the future, deeper imaging with NIRCam and NIRSpec spectroscopy should become available for many of the sources in our $z \geq 8$ selections from the JADES program, e.g. as in Curtis-Lake et al. (2022) and Robertson et al. (2022). This will allow for a more sensitive probe down the *UV* LFs at $z \geq 8$ and also a search for fainter sources to even higher redshift. Additionally, it should facilitate spectroscopic confirmation and characterization of the faint $z \geq 8$ galaxies located within the HUDF, providing essential insight into the sources that likely reionized the universe (e.g. Bouwens et al. 2015b; Robertson 2022).

ACKNOWLEDGEMENTS

DATA AVAILABILITY

All data used here are available from the *Barbara A Mikulski Archive for Space Telescopes* (*MAST*: https://mast.stsci.edu), both in the form of raw and high level science products.

REFERENCES

Adams N. J. et al., 2023, MNRAS, 518, 4755
Anders P., Fritze-v. Alvensleben U., 2003, A&A, 401, 1063
Atek H. et al., 2023, MNRAS, 519, 1201
Bagley M. B. et al., 2022, preprint (arXiv:2205.12980)
Beckwith S. V. W. et al., 2006, AJ, 132, 1729
Behroozi P. S., Wechsler R. H., Conroy C., 2013, ApJ, 770, 57
Bertin E., Arnouts S., 1996, A&AS, 117, 393
Bhatawdekar R., Conselice C. J., Margalef-Bentabol B., Duncan K., 2019, MNRAS, 486, 3805
Bouwens R. et al., 2020, ApJ, 902, 112
Bouwens R. J. et al., 2011a, Nature, 469, 504
Bouwens R. J. et al., 2011b, ApJ, 737, 90
Bouwens R. J. et al., 2013, ApJ, 765, L16
Bouwens R. J. et al., 2014a, ApJ, 793, 115
Bouwens R. J. et al., 2014b, ApJ, 795, 126
Bouwens R. J. et al., 2015a, ApJ, 803, 34
Bouwens R. J., Illingworth G. D., Oesch P. A., Caruana J., Holwerda B., Smit R., Wilkins S., 2015b, ApJ, 811, 140
Bouwens R. J. et al., 2016a, ApJ, 830, 67
Bouwens R. J. et al., 2016b, ApJ, 833, 72
Bouwens R. J., Stefanon M., Oesch P. A., Illingworth G. D., Nanayakkara T., Roberts-Borsani G., Labbé I., Smit R., 2019, ApJ, 880, 25
Bouwens R. J. et al., 2021, AJ, 162, 47
Bouwens R., Illingworth G., Oesch P., Stefanon M., Naidu R., van Leeuwen I., Magee D., 2022a, preprint (arXiv:2212.06683)
Bouwens R. J. et al., 2022b, ApJ, 931, 160
Bowler R. A. A., Jarvis M. J., Dunlop J. S., McLure R. J., McLeod D. J., Adams N. J., Milvang-Jensen B., McCracken H. J., 2020, MNRAS, 493, 2059
Boylan-Kolchin M., 2022, preprint (arXiv:2208.01611)
Bradley L. D. et al., 2022, preprint (arXiv:2210.01777)
Brammer G., 2023, grizli, Zenodo, available at: https://zenodo.org/record/7767790#.ZFSnX3ZBzIU
Brammer G. B., van Dokkum P. G., Coppi P., 2008, ApJ, 686, 1503
Brammer G. B., van Dokkum P. G., Illingworth G. D., Bouwens R. J., Labbé I., Franx M., Momcheva I., Oesch P. A., 2013, ApJ, 765, L2
Bruzual G., Charlot S., 2003, MNRAS, 344, 1000
Bunker A. J., NIRSPEC Instrument Science Team, JADES Collaboration, 2020, in da Cunha E., Hodge J., Afonso J., Pentericci L., Sobral D.eds, Proc. IAU Vol. 352, Uncovering Early Galaxy Evolution in the ALMA and JWST Era. p. 342
Burgasser A. J., 2014, in Singh H. P., Prugniel P., Vauglin I., eds, ASI Conf. Ser. Vol. 11, International Workshop on Stellar Spectral Libraries. p. 7
Byler N., Dalcanton J. J., Conroy C., Johnson B. D., 2017, ApJ, 840, 44
Calvi V. et al., 2016, ApJ, 817, 120
Calzetti D., Armus L., Bohlin R. C., Kinney A. L., Koornneef J., Storchi-Bergmann T., 2000, ApJ, 533, 682
Carnall A. C., McLure R. J., Dunlop J. S., Davé R., 2018, MNRAS, 480, 4379
Carnall A. C. et al., 2023, MNRAS, 518, L45
Castellano M. et al., 2022, ApJ, 938, L15
Chabrier G., 2003, PASP, 115, 763
Choi J., Dotter A., Conroy C., Cantiello M., Paxton B., Johnson B. D., 2016, ApJ, 823, 102
Coe D. et al., 2013, ApJ, 762, 32
Coleman G. D., Wu C. C., Weedman D. W., 1980, ApJS, 43, 393
Conroy C., Gunn J. E., 2010, ApJ, 712, 833
Conroy C., Wechsler R. H., 2009, ApJ, 696, 620
Cullen F. et al., 2023, MNRAS, 520, 14
Curtis-Lake E. et al., 2022, preprint (arXiv:2212.04568)
Davidzon I., Ilbert O., Faisst A. L., Sparre M., Capak P. L., 2018, ApJ, 852, 107
De Barros S., Oesch P. A., Labbé I., Stefanon M., González V., Smit R., Bouwens R. J., Illingworth G. D., 2019, MNRAS, 489, 2355
Dekel A., Zolotov A., Tweed D., Cacciato M., Ceverino D., Primack J. R., 2013, MNRAS, 435, 999
Donnan C. T. et al., 2023, MNRAS, 518, 6011
Dotter A., 2016, ApJS, 222, 8
Duncan K. et al., 2014, MNRAS, 444, 2960
Dunlop J. S. et al., 2013, MNRAS, 432, 3520
Dunlop J. S. et al., 2017, MNRAS, 466, 861
Ellis R. S. et al., 2013, ApJ, 763, L7
Endsley R., Stark D. P., Chevallard J., Charlot S., 2021, MNRAS, 500, 5229
Endsley R., Stark D. P., Whitler L., Topping M. W., Chen Z., Plat A., Chisholm J., Charlot S., 2022, preprint (arXiv:2208.14999)
Faisst A. L. et al., 2016, ApJ, 821, 122
Ferland G. J. et al., 2013, RMxAA, 49, 137
Ferrara A., Pallottini A., Dayal P., 2022, preprint (arXiv:2208.00720)
Finkelstein S. L. et al., 2013, Nature, 502, 524
Finkelstein S. L. et al., 2017, The Cosmic Evolution Early Release Science (CEERS) Survey, JWST Proposal ID 1345. Cycle 0 Early Release Science
Finkelstein S. L. et al., 2022a, ApJL, 940, L55
Finkelstein S. L. et al., 2022b, ApJ, 928, 52
Furtak L. J., Atek H., Lehnert M. D., Chevallard J., Charlot S., 2021, MNRAS, 501, 1568
Furtak L. J., Shuntov M., Atek H., Zitrin A., Richard J., Lehnert M. D., Chevallard J., 2023, MNRAS, 519, 3064
Genel S. et al., 2014, MNRAS, 445, 175
Giavalisco M. et al., 2004, ApJ, 600, L93
González V., Labbé I., Bouwens R. J., Illingworth G., Franx M., Kriek M., 2011, ApJ, 735, L34
Grazian A. et al., 2015, A&A, 575, A96
Harikane Y. et al., 2022, ApJS, 259, 20
Harikane Y. et al., 2023, ApJS, 265, L5
Hashimoto T. et al., 2018, Nature, 557, 392
Illingworth G. D. et al., 2013, ApJS, 209, 6
Inayoshi K., Harikane Y., Inoue A. K., Li W., Ho L. C., 2022, ApJ, 938, L10
Ishigaki M., Kawamata R., Ouchi M., Oguri M., Shimasaku K., Ono Y., 2018, ApJ, 854, 73
Jiang L. et al., 2021, Nature Astron., 5, 256
Johnson B. D., Leja J., Conroy C., Speagle J. S., 2021, ApJS, 254, 22
Kannan R. et al., 2022, preprint (arXiv:2210.10066)
Khusanova Y. et al., 2020, A&A, 634, A97
Kikuchihara S. et al., 2020, ApJ, 893, 60
Koekemoer A. M. et al., 2013, ApJS, 209, 3
Kotulla R., Fritze U., Weilbacher P., Anders P., 2009, MNRAS, 396, 462
Kron R. G., 1980, ApJS, 43, 305
Labbé I. et al., 2013, ApJ, 777, L19
Labbe I. et al., 2023, Nature, 616, 266
Lam D. et al., 2019, preprint (arXiv:1903.08177)
Leethochawalit N., Roberts-Borsani G., Morishita T., Trenti M., Treu T., 2022, preprint (arXiv:2205.15388)

Leethochawalit N. et al., 2023, ApJL, 942, L26

Leja J., Carnall A. C., Johnson B. D., Conroy C., Speagle J. S., 2019a, ApJ, 876, 3

Leja J. et al., 2019b, ApJ, 877, 140

Leja J. et al., 2022, ApJ, 936, 165

Livermore R. C., Trenti M., Bradley L. D., Bernard S. R., Holwerda B. W., Mason C. A., Treu T., 2018, ApJ, 861, L17

Lovell C. C., Harrison I., Harikane Y., Tacchella S., Wilkins S. M., 2023, MNRAS, 518, 2511

Madau P., Dickinson M., 2014, ARA&A, 52, 415

Mármol-Queraltó E., McLure R. J., Cullen F., Dunlop J. S., Fontana A., McLeod D. J., 2016, MNRAS, 460, 3587

Mason C. A., Trenti M., Treu T., 2015, ApJ, 813, 21

Mason C. A., Trenti M., Treu T., 2023, MNRAS, 521, 497

Mawatari K. et al., 2020, ApJ, 889, 137

McLeod D. J., McLure R. J., Dunlop J. S., 2016, MNRAS, 459, 3812

McLure R. J. et al., 2013, MNRAS, 432, 2696

McLure R. J. et al., 2018, MNRAS, 476, 3991

Mirocha J., Furlanetto S. R., 2023, MNRAS, 519, 843

Morishita T., 2021, ApJS, 253, 4

Morishita T. et al., 2018, ApJ, 867, 150

Naidu R. P. et al., 2022, preprint (arXiv:2208.02794)

Naidu R. P. et al., 2023, ApJL, 940, L14

Neistein E., Dekel A., 2008, MNRAS, 388, 1792

Oesch P. A. et al., 2013, ApJ, 773, 75

Oesch P. A. et al., 2014, ApJ, 786, 108

Oesch P. A. et al., 2015, ApJ, 804, L30

Oesch P. A. et al., 2016, ApJ, 819, 129

Oesch P. A., Bouwens R. J., Illingworth G. D., Labbé I., Stefanon M., 2018, ApJ, 855, 105

Oke J. B., Gunn J. E., 1983, ApJ, 266, 713

Ono Y. et al., 2012, ApJ, 744, 83

Ono Y. et al., 2022, preprint (arXiv:2208.13582)

Pontoppidan K. M. et al., 2022, ApJ, 936, L14

Reddy N. A., Steidel C. C., 2009, ApJ, 692, 778

Roberts-Borsani G. W. et al., 2016, ApJ, 823, 143

Roberts-Borsani G. W., Ellis R. S., Laporte N., 2020, MNRAS, 497, 3440

Roberts-Borsani G., Morishita T., Treu T., Leethochawalit N., Trenti M., 2022, ApJ, 927, 236

Robertson B. E., 2022, ARA&A, 60, 121

Robertson B. E. et al., 2022, ARA&A, 60, 121

Robertson B. E., Ellis R. S., Furlanetto S. R., Dunlop J. S., 2015, ApJ, 802, L19

Rodighiero G., Bisigello L., Iani E., Marasco A., Grazian A., Sinigaglia F., Cassata P., Gruppioni C., 2023, MNRAS, 518, L19

Rojas-Ruiz S., Finkelstein S. L., Bagley M. B., Stevans M., Finkelstein K. D., Larson R., Mechtley M., Diekmann J., 2020, ApJ, 891, 146

Salmon B. et al., 2015, ApJ, 799, 183

Santini P. et al., 2017, ApJ, 847, 76

Schaerer D., Marques-Chaves R., Barrufet L., Oesch P., Izotov Y. I., Naidu R., Guseva N. G., Brammer G., 2022, A&A, 665, L4

Smit R. et al., 2014, ApJ, 784, 58

Smit R. et al., 2015, ApJ, 801, 122

Song M. et al., 2016, ApJ, 825, 5

Stark D. P., Ellis R. S., Bunker A., Bundy K., Targett T., Benson A., Lacy M., 2009, ApJ, 697, 1493

Stark D. P., Ellis R. S., Chiu K., Ouchi M., Bunker A., 2010, MNRAS, 408, 1628

Stark D. P. et al., 2017, MNRAS, 464, 469

Stefanon M. et al., 2019, ApJ, 883, 99

Stefanon M., Bouwens R. J., Labbé I., Muzzin A., Marchesini D., Oesch P., Gonzalez V., 2017, ApJ, 843, 36

Stefanon M., Bouwens R. J., Labbé I., Illingworth G. D., Gonz alez V., Oesch P. A., 2021, ApJ, 922, 29

Stefanon M., Bouwens R. J., Labbé I., Illingworth G. D., Oesch P. A., van Dokkum P., Gonzalez V., 2022a, ApJ, 927, 48

Stefanon M., Bouwens R. J., Illingworth G. D., Labbé I., Oesch P. A., Gonzalez V., 2022b, ApJ, 935, 94

Stefanon M., Bouwens R. J., Labbé I., Illingworth G. D., Gonz alez V., Oesch P. A., 2023, ApJ, 943, 81

Steidel C. C., Adelberger K. L., Giavalisco M., Dickinson M., Pettini M., 1999, ApJ, 519, 1

Steidel C. C., Adelberger K. L., Shapley A. E., Pettini M., Dickinson M., Giavalisco M., 2003, ApJ, 592, 728

Steinhardt C. L., Kokorev V., Rusakov V., Garcia E., Sneppen A., 2022, preprint (arXiv:2208.07879)

Strait V. et al., 2020, ApJ, 888, 124

Szalay A. S., Connolly A. J., Szokoly G. P., 1999, AJ, 117, 68

Tacchella S., Bose S., Conroy C., Eisenstein D. J., Johnson B. D., 2018, ApJ, 868, 92

Tacchella S. et al., 2022, ApJ, 927, 170

Teplitz H. I. et al., 2013, AJ, 146, 159

Thompson R. I. et al., 2005, AJ, 130, 1

Topping M. W., Stark D. P., Endsley R., Plat A., Whitler L., Chen Z., Charlot S., 2022a, ApJ, 941, 153

Topping M. W. et al., 2022b, MNRAS, 516, 975

Trenti M., Stiavelli M., 2008, ApJ, 676, 767

Treu T. et al., 2022, ApJ, 935, 110

Weinmann S. M., Neistein E., Dekel A., 2011, MNRAS, 417, 2737

Whitler L., Stark D. P., Endsley R., Leja J., Charlot S., Chevallard J., 2023a, MNRAS, 519, 157

Whitler L., Stark D. P., Endsley R., Leja J., Charlot S., Chevallard J., 2023b, MNRAS, 519, 5859

Wilkins S. M. et al., 2023, MNRAS, 518, 3935

Wilkins S. M., Bouwens R. J., Oesch P. A., Labbé I., Sargent M., Caruana J., Wardlow J., Clay S., 2016, MNRAS, 455, 659

Williams C. C. et al., 2023, preprint (arXiv:2301.09780)

Yan H., Ma Z., Ling C., Cheng C., Huang J.-s., Zitrin A., 2023, ApJL, 942, L9

Yu-Yang Hsiao T. et al., 2022, preprint (arXiv:2210.14123)

Zavala J. A. et al., 2023, ApJL, 943, L9

Zitrin A. et al., 2014, ApJ, 793, L12

Zitrin A. et al., 2015, ApJ, 810, L12

APPENDIX A: POSTAGE STAMPS AND SEDS FOR CURRENT SAMPLE OF z ∼ 8−9 GALAXIES

Here we present the postage stamp images and model SEDs we derive for the present selection of z ∼ 8–9 galaxies identified over the HUDF. The postage stamp images are presented in Fig. A1 while the best-fitting model SEDs for these sources are presented in Fig. A2.
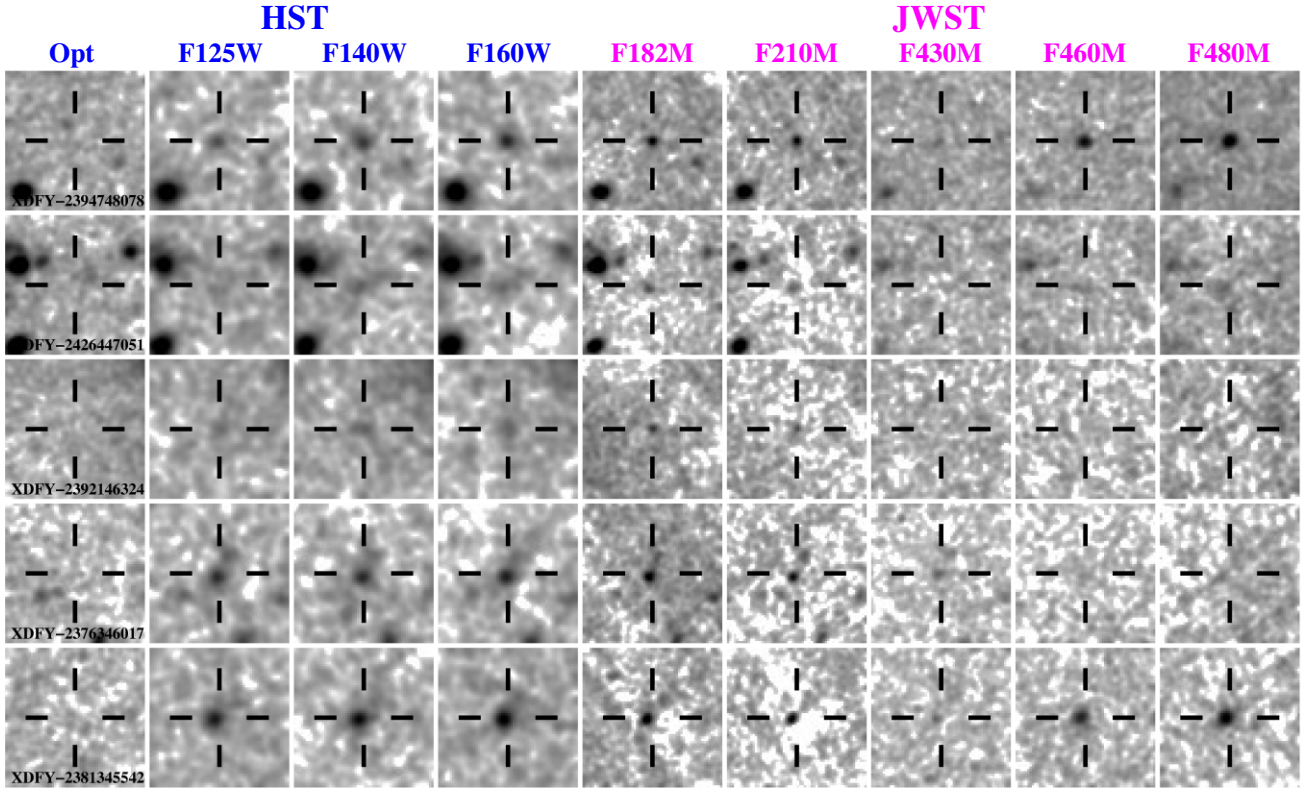
Figure A1. Similar to Fig. 7 but for the five $z \sim 8$–9 galaxy candidates in our selection. All five candidate had been identified as part of earlier $z \sim 8$–9 selections over the HUDF. The particularly bright detections in the F460M and F480M bands for two sources from this selection, XDFY-2394648078 and XDFY2381345542, almost certainly arise due to line emission from [O III] +Hβ, allowing us to place very tight constraints on their photometric redshifts as well as the EW of the [O III] + Hβ lines (see Fig. 11).
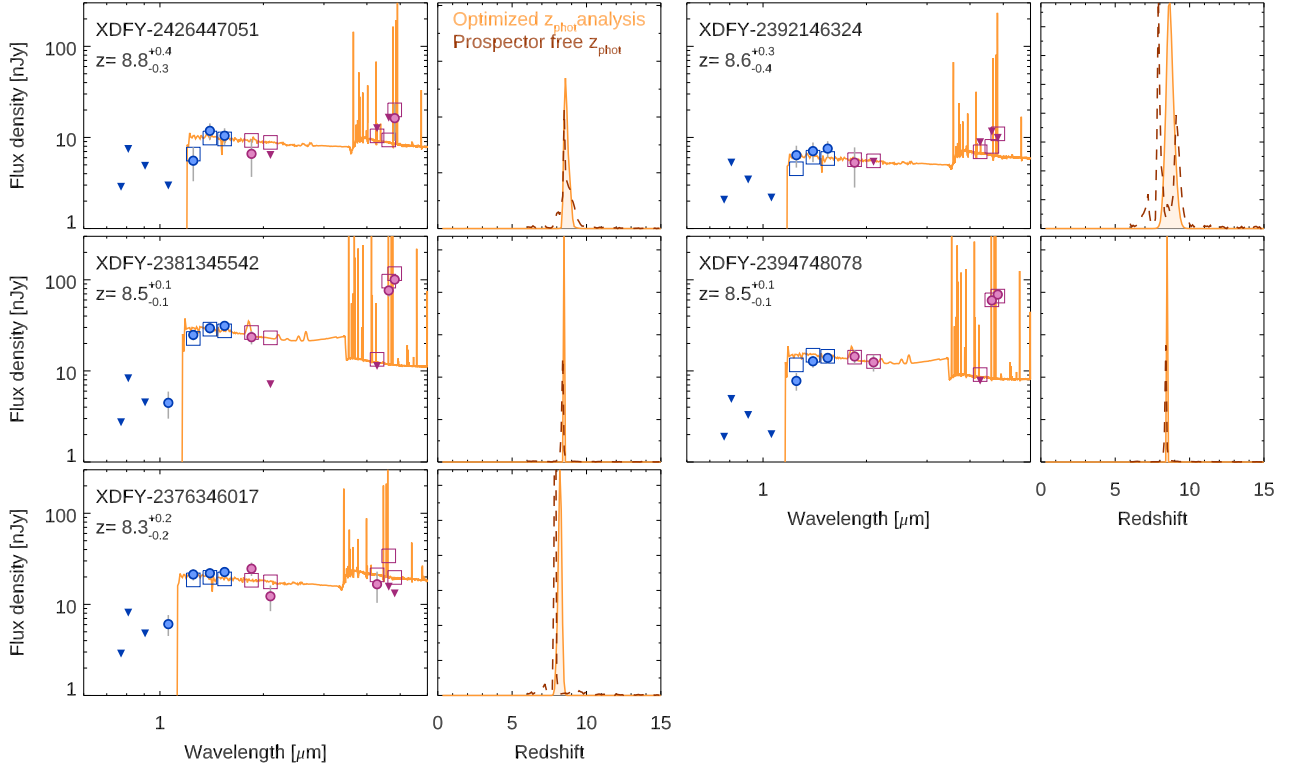
Figure A2. Similar to Fig. 5 but for galaxies in our $z \sim 8$–9 sample. Note the dramatic differences in the tightness of the redshift constraints on $z \sim 8$–9 sources with prominent line emission contributing to the medium bands (e.g. XDFY-2381345542 and XDFY-2394748078) and those sources without such emission (e.g. XDFY-2392146324).

APPENDIX B: ANALYSIS OF VARIOUS $z = 8$–10 CANDIDATE GALAXIES PREVIOUSLY REPORTED IN THE LITERATURE

Here we consider various $z = 8$–10 candidate galaxies which had previously been reported in various analyses but did not meet the current selection criteria. These sources were derived from a number of previous analyses of the HUDF including Bouwens et al. (2011a, 2013, 2015a), Ellis et al. (2013), McLure et al. (2013), and Oesch et al. (2013). There are eight such sources, and they are listed in Table B1 with source IDs running from C1 to C8.

For our assessment, we place 0.35 arcsec diameter apertures at the reported coordinate of the sources (after accounting for the 0.3 arcsec shift in the coordinates of the sources to account for the improved astrometry of the HUDF data) but otherwise compute total magnitudes using scalable Kron apertures corrected to total using the estimated encircled energy on the wings of the JWST F182M-band PSF.

Table B1. $z \geq 8.5$ candidate Galaxies previously identified over the HUDF/XDF.

ID	RA	DEC	z_{phot}^a	m_{UV} [mag][b]	Lyman break [mag][c]	$\Delta\chi^{2a,d}$	$p(z>5.5)^a$	Lit[1]
C1	03:32:38.95	−27:47:11.7	–	>30.0	–	–	–	E13
C2	03:32:39.44	−27:46:32.0	$7.8^{+1.2}_{-1.1}$	29.8 ± 0.5	>1.2	−3.7	0.901	O13
C3	03:32:38.27	−27:45:56.4	$8.0^{+0.3}_{-0.3}$	29.8 ± 0.5	>1.9	−12.0	0.994	B15
C4	03:32:43.69	−27:46:40.9	$8.2^{+1.2}_{-0.8}$	29.4 ± 0.7	0.0 ± 1.5	−0.1	0.712	B11
C5	03:32:37.79	−27:46:00.4	$8.2^{+0.2}_{-0.2}$	28.2 ± 0.1	1.5 ± 0.2	−40.8	1.000	M13,B15
C6	03:32:35.43	−27:47:33.8	$8.5^{+1.1}_{-1.0}$	29.6 ± 0.3	>0.9	−0.2	0.546	B11
C7	03:32:43.45	−27:46:54.9	$9.1^{+0.5}_{-0.4}$	29.6 ± 0.4	>1.3	−12.7	0.999	E13,M13,O13
C8	03:32:41.07	−27:47:30.7	–	>30.0	–	–	–	E13

[1] B11 = Bouwens et al. (2011a), E13 = Ellis et al. (2013), M13 = McLure et al. (2013), O13 = Oesch et al. (2013), B15 = Bouwens et al. (2015a)

[a] Derived using EAzY (Brammer et al. 2008)

[b] Derived using the flux in the H_{160}, HK_{182}, and K_{210} bands for sources in our $z \sim 8$–9, $z \sim 10$–11, and $z \sim 12$–13 samples to probe the UV luminosity at ≈ 1600 Å rest-frame.

[c] Amplitude of the nominal Lyman breaks for these $z \geq 8$ galaxy candidates.
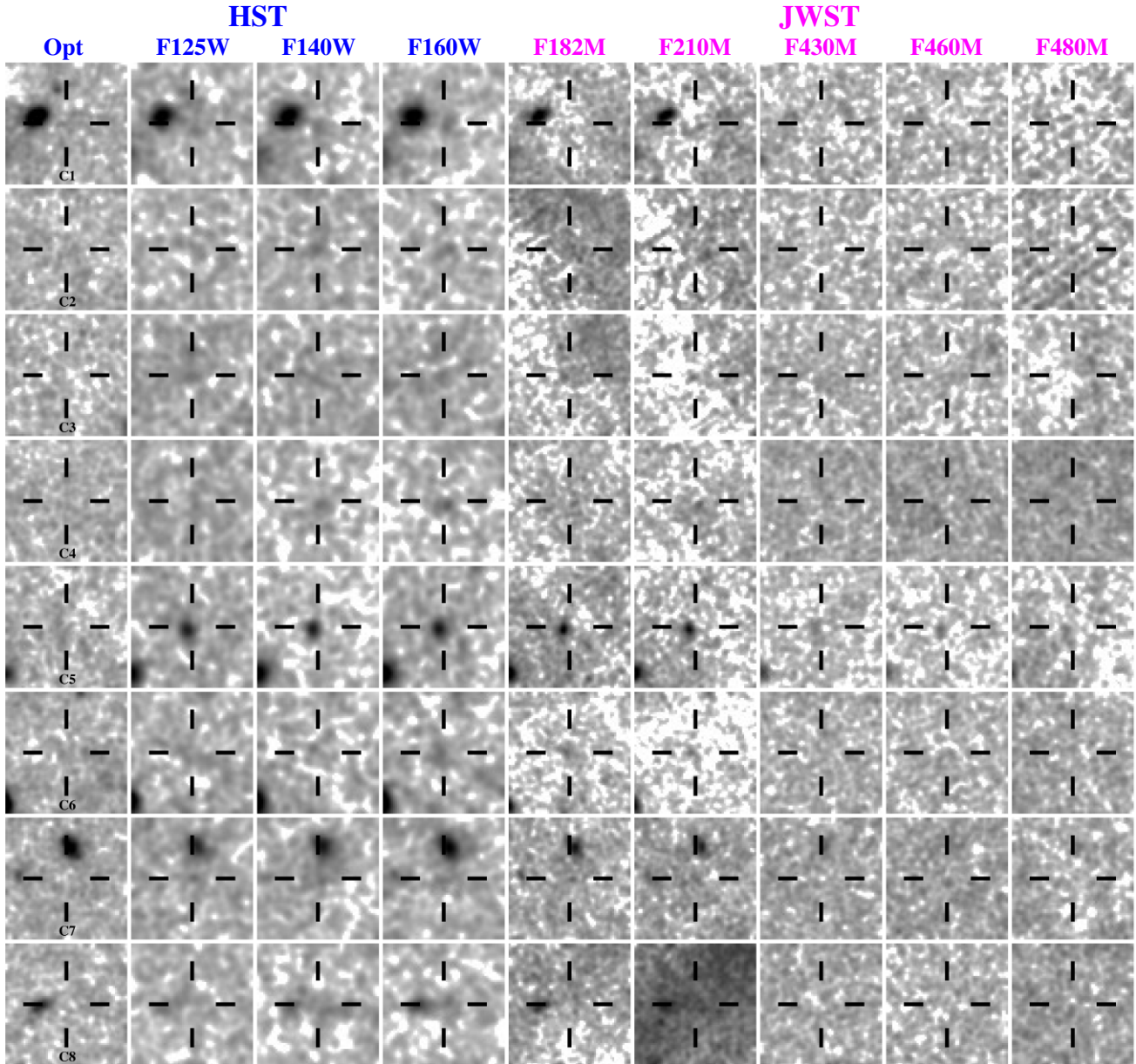
[d] $\chi^2_{best,z>5.5} - \chi^2_{best,z<5.5}$

Figure B1. Similar to Fig. 7 but showing various candidate $z = 8-11$ galaxies that had been previously reported in the literature but which were not recovered using the current selection criteria. While six of the eight candidate show $\geq 2\sigma$ detections in the F182M and F210M bands, two candidates notably show no apparent flux in the new data from *JWST* and may be spurious. The characteristics of the sources we derive from SED fits to our photometry are presented in Table B1.

Postage stamps of the eight candidates are shown in Fig. B1, and only three of the eight show clear $\geq 2\sigma$ detections in both the F182M and F210M images. While the NIRCam imaging observations nevertheless support the reality of three of the remaining five, the NIRCam imaging observations provide no support for the reality of two of the candidates C1 and C8. Since one of these candidates C8 was already suspected to show apparent flux from a diffraction spike and thus likely to be spurious (see discussion in Oesch et al. 2013), the new observations appear to confirm that this interpretation was correct. The absence of a detection in the F182M and F210M bands for the second candidate C1 is surprising given the apparent detection of the source at $>3.5\sigma$ in the WFC3/IR F140W and F160W bands (Ellis et al. 2013; Oesch et al. 2013). However, the lack of apparent flux in the new NIRCam data suggests this source may have either been spurious or variable.

Using the same SED templates from EAzY (Brammer et al. 2008) to compute the redshift likelihood distribution for the six sources that appear to be real on the basis of the new NIRCam observations, we present our results in Fig. B2. Our likelihood analysis suggests that five of the six remaining candidates (C2, C3, C4, C5, C7) are very likely at $z \geq 8$, but with larger uncertainties regarding the nature of C6 earlier reported by Bouwens et al. (2011a).

Of the five candidates that appear likely to be at $z \geq 8$, three did not make it into our selection due to the F182M + F210M medium band fluxes' showing less than 2σ detections. A fourth candidate C5 did not make it into our selection because it was detected at $>5\sigma$ significance in the Y_{105} band and thus excluded. A fifth candidate C7 was excluded because it did not make it into the SEXTRACTOR catalog we used to assemble our $z \geq 8$ selection over the HUDF, but appears to otherwise satisfy our selection criteria.
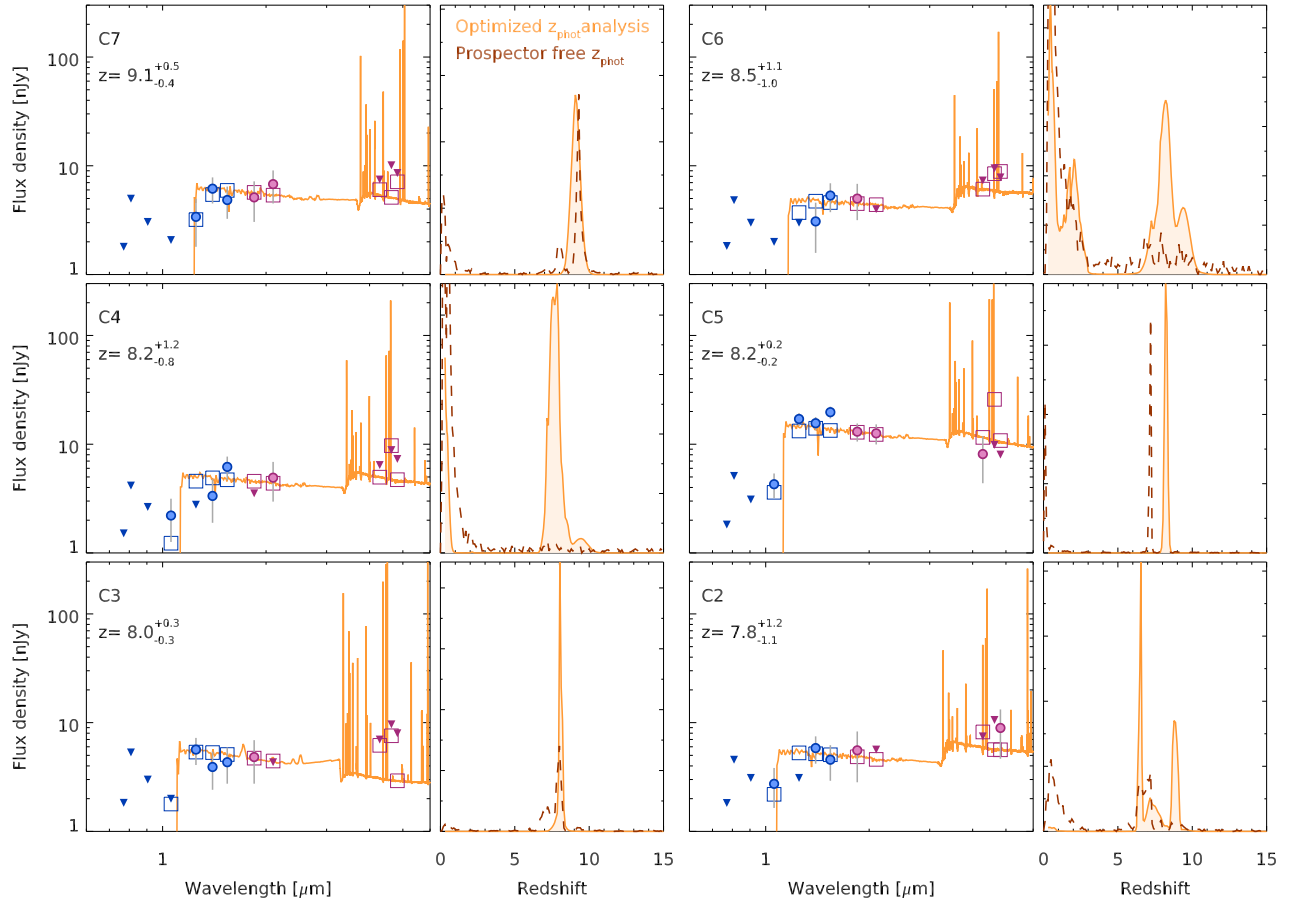
Figure B2. Similar to Fig. A2 but for various candidate $z = 8$–11 galaxies which had previously been reported in the literature but are not recovered using the selection criteria used here. The characteristics of the sources we derive from SED fits to our photometry are presented in Table B1.

This paper has been typeset from a TEX/LATEX file prepared by the author.